Large-eddy simulations of complex aerodynamic flows over multi-element iced airfoils

Young Mo Lee[a], Jae Hwa Lee[a,b,*], Lawrence Prince Raj[c], Je Hyun Jo[d], Rho Shin Myong[b,d]

[a] *Department of Mechanical Engineering, Ulsan National Institute of Science and Technology (UNIST), 50 UNIST-gil, Eonyang-eup, Ulsan 44919, Korea*
[b] *Research Center for Aircraft Care Technology and ReCAPT, Gyeongsang National University, Jinju, Gyeongnam 52828, Korea*
[c] *Department of Aerospace Engineering and Applied Mechanics, Indian Institute of Engineering Science and Technology, Shibpur, Howrah-711103, West Bengal, India*
[d] *School of Aerospace and Software Engineering, Gyeongsang National University, Jinju, Gyeongnam 52828, Korea*

Abstract

Large-eddy simulations (LESs) of flows over two types of iced airfoils with three multi-elements are performed to investigate the aerodynamic characteristics and complex interactions between flows generated from slat, main, and flap elements. The two iced airfoils are considered under supercooled large droplet (SLD) and non-SLD conditions. A good agreement of the mean properties between our numerical and previous experimental data demonstrates that our LES method provides an accurate solution of the complex flows around iced airfoils., whereas it is not for unsteady Reynolds-averaged Navier–Stokes (URANS) data that is simulated independently. For the iced airfoils under the SLD and non-SLD conditions, the aerodynamic degradation is found compared to that of a clean airfoil because the separation bubbles (SBs) induced by ice accretion change shear layer (SL) trajectory shed from the slat cusp, leading to a severe reduction in mass flow. Furthermore, we show that the flow interactions near the slat gap play a crucial role in determining the flow characteristics on main and flap elements (e.g., flow separation). Although strong flow interactions are observed for the non-SLD case because of the presence of upwind horn-shaped ice, the smaller gap distance of the SLD case leads to a larger lift loss. The unsteady features of SBs on the upper surfaces of the slat and main elements

---

[*] Corresponding author.
Email address: jhlee06@unist.ac.kr (J.H. Lee).

under the non-SLD condition are characterized by the power spectral density (PSD) of the pressure fluctuations with multiple peaks at low and high frequencies.

Keywords: Large-eddy simulation, Multi-element iced airfoil, Aerodynamics

---

1. Introduction

The supercooled water droplets available in clouds can result in ice accretion on the surfaces of aircrafts and engines when an aircraft flies at subfreezing temperatures. The ice accretion shapes are affected by atmospheric temperature, liquid–water content (LWC), median volume diameter (MVD) of droplet, flight speed, and phase of flight, and the accreted ice leads to a severe reduction in lift, increased drag, and aircraft instability [1-4]. Furthermore, the droplet diameter is known to have strong influence on the amount, location, and shape of the ice accretion [5-7]. In the aviation community, the droplet diameter in the range of 40 μm or less has been considered for certification (FAA Appendix C). However, in some atmospheric conditions the droplet size may reach 40 μm to 400 μm, which is known as a supercooled large droplet (SLD). Hence, in 2014, a new certification regulation is added (Appendix O) along with the present regulations (Appendix C) to address the effect of SLD icing conditions. Because an investigation of ice shapes generated under various conditions along with aerodynamic performance is essential for the certification process and ice protection system design, it is valuable to study the effects of icing on the aerodynamics around various iced airfoils.

For several decades, much effort has been devoted to the study of flows around single-element iced airfoils [1,8-11]. However, since modern aircraft usually use multi-element wings to attain high lift at a high angle of attack (AOA) and low speeds [12], recent studies have examined the effects of ice accretion on multi-element airfoils with a supercooled large droplet (SLD) greater than 40 μm and/or a non-SLD smaller than 40 μm. In the NASA Lewis Icing Research Tunnel (IRT), Shin et al. [13] analyzed the effects of droplet size on a multi-element airfoil under a non-SLD condition. They employed two median volume diameters (MVDs) of 20 and 25 μm and showed that the icing limits generated with a larger MVD move further downstream on both the upper and lower surfaces despite a slight spread. Miller et al. [14] investigated the influence of the flap gap distance on ice accretion with a 20-μm MVD using three flap-gap sizes (1.52%, 1.75%, and 2.02% chord). They reported that changing the flap gap has a small effect on ice accretion over a multi-element iced airfoil compared to that of the AOA. Under a SLD condition, Zhang et al. [15] simulated flows around multi-element airfoils using three large droplet sizes (MVD = 50, 200, and 400 μm) to investigate the aerodynamic features. They found that the lift loss with a higher MVD is significantly greater for all elements (i.e., slat, main, and flap elements), similar to earlier observations for single-element iced airfoils [16-17]. Recently, Raj et al. [18] conducted numerical simulations of flows over multi-element iced airfoils under both SLD (MVD = 92 and 154 μm) and non-SLD (MVD = 30 μm) conditions. The variation of the lift and drag coefficients showed a higher aerodynamic degradation under a non-SLD condition than under a SLD icing condition because the horn-shaped ice on the main element under the non-SLD condition significantly decreased the aerodynamic performance of the main element. This result is contrary to earlier observations for single- and multi-element iced airfoils [15-17].

Many previous numerical studies have been performed to investigate unsteady flows over iced airfoils using the Reynolds-averaged Navier–Stokes (RANS) method [19-21]. However, this method overestimates the pressure coefficient on the upper surface and underestimates the stall angle and lift coefficient because it cannot correctly resolve the separation bubbles (SBs), which are an important phenomenon that determines the aerodynamic performance on an iced airfoil [1]. As a remedy, Brown et al. [9] showed that an implicit LES method provides a better prediction of the lift coefficient as a function of the AOA than that of the RANS simulations. Pan and Loth [19] reported that the detached-eddy simulation (DES) method provides a more accurate prediction of the maximum lift coefficient and stall angle than the RANS method, similar to previous observations [22-23]. However, the prediction of the DES method is poor on the Kelvin–Helmholtz (K-H) instability for a mixing shear layer, although the prediction of K-H instability is a key issue for the accurate prediction of SBs over iced airfoils [11]. Furthermore, the zonal detached-eddy simulations (ZDES) have been applied to prediction of flows over iced airfoils [10, 24-25]. Zhang et al. [10] showed that the ZDES provides a better prediction on pressure distribution and lift than the RANS approach, although a small difference was observed in the surface pressure between the ZDES and experimental data. Recently, Deck and Renard [26] proposed a new ZDES method to ensure a RANS mode in attached boundary layers for any mesh size without an excessive delay in the resolved LES content and formation of instabilities. The profiles of skin friction, eddy viscosity and mean velocity from the proposed method in a flat-plate turbulent boundary layer flow under an infinitely fine mesh demonstrated that an improved shielding function of the proposed method leads to a better prediction performance than that of the original delayed detached-eddy simulation (DDES) [27] and ZDES [28].

Although the flows over single-element iced airfoils with a wide range of droplet sizes are understood, a detailed analysis of the flow fields around multi-element iced airfoils is lacking because of the wide range of geometrical parameters and complicated flow features [15,18]. Furthermore, although unsteady turbulent motions are closely related to the aerodynamic features [29-30], most previous studies have focused on the analysis of only the mean (steady) properties of multi-element iced airfoils [13-14,18,31]. Thus, it is necessary step to study flow fields around a multi-element iced airfoil with slat and flap elements to gain a better understanding of their aerodynamic characteristics. In this study, the accurate prediction of unsteady complex flows around multi-element iced airfoils using LES is performed to provide valuable insight on their aerodynamics. Iced airfoils under SLD and non-SLD conditions are taken into account, and results are compared with those of a clean airfoil to identify unique aerodynamic characteristics. In addition to LES, we have performed unsteady RANS (URANS) simulations to highlight the differences between the LES and URANS data. In the following, the flow characteristics under the influences of ice shapes and AOA are investigated by considering the lift coefficient, ratio of lift to drag, pressure coefficient, mean velocity, streamlines, and Reynolds stresses. In addition, instantaneous flow fields using velocity magnitude and time-evolving spanwise vorticity are analyzed to scrutinize complex flow interactions.

Finally, a spectral analysis of pressure fluctuations is performed in highly unsteady regions to identify the dominant frequencies of unsteady flows.

2. Computational details

2.1. *Numerical method*

ANSYS Fluent 17.1 (Ansys Inc., PA, USA) is utilized for all simulations in this study. The good prediction performances of LESs for turbulent flows based on the ANSYS Fluent code have been validated by previous studies [32-33]. For a compressible flow, a density-based solver is used for three-dimensional and unsteady conditions. The computational domain is discretized through the finite volume method (FVM). The filtered Navier–Stokes (NS) equations are solved by the second-order upwind scheme. Temporal discretization is fully implicit with second-order accuracy for unsteady flow calculations. To solve the filtered NS equations, the convective fluxes are computed by Roe flux-difference splitting (Roe-FDS) scheme [34], and the gradients of the solution variables at the cell centers are determined using the least-squares cell-based method [35]. The coordinate system is such that x ($=x_1$), y ($=x_2$) and z ($=x_3$) denote the streamwise, crosswise, and spanwise coordinates, respectively, and that $\overline{u}$ ($= \overline{u}_1$), $\overline{v}$ ($= \overline{u}_2$), and $\overline{w}$ ($= \overline{u}_3$) indicate the corresponding velocity components. The overbar denotes the implicit filter that determines the resolved scales, and the filtering operation is implicitly done by finite volume discretization. In the following equations, a bracket $\langle \cdot \rangle$ and capital letters (e.g., U) indicate temporally averaged statistics. The superscript + indicates quantities normalized by the local mean friction velocity on the wall (U_τ), and the velocity fluctuations ($\overline{u}_i^{'}$) are calculated as $\overline{u}_i^{'} = \overline{u}_i - < \overline{u}_i >$.

For a compressible flow, it is useful to recast variables in terms of Favre-filtered quantities. Thus, the variables employed in the present study are defined using the Favre (or density weighted) filtering operator $\tilde{f} = \overline{\rho f} / \overline{\rho}$. In the Favre-filtered NS equations for compressible flows, the effects of the unresolved subgrid scale (SGS) in the momentum equations are modeled in SGS stress terms, τ_{ij} , [36] as

$$\tau_{ij} = \bar{\rho}\left(\widetilde{u_i u_j} - \tilde{u}_i \tilde{u}_j\right), \tag{1}$$

where the tilde (~) indicates the Favre filter. The velocity u_i can be decomposed as

$$u_i = \tilde{u}_i + u_i^s. \tag{2}$$

When substituting Eq. (2) into Eq. (1), we obtain the classical decomposition of the SGS stress tensor as

$$\tau_{ij} = L_{ij} + C_{ij} + R_{ij}, \tag{3}$$

where

$$\begin{aligned} L_{ij} &= \bar{\rho}\left(\widetilde{\tilde{u}_i \tilde{u}_j} - \tilde{u}_i \tilde{u}_j\right), \\ C_{ij} &= \bar{\rho}\left(\widetilde{u_i^s \tilde{u}_j} + \widetilde{\tilde{u}_i u_j^s}\right) \text{ and} \\ R_{ij} &= \bar{\rho}\widetilde{u_i^s u_j^s}. \end{aligned} \tag{4}$$

L_{ij} , C_{ij} , and R_{ij} are the Leonard stress, cross-stress, and SGS Reynolds stress, respectively.

In the present LES, the dynamic Smagorinsky model [36-39] is applied to calculate the SGS stress tensor τ_{ij} for the effect of unresolved scales. The anisotropic part of the SGS stress tensor is assumed as:

$$\tau_{ij} - \frac{\delta_{ij}}{3}\tau_{kk} = -2\left(C_S\bar{\Delta}\right)^2 \bar{\rho}\left|\tilde{S}\right|\left(\tilde{S}_{ij} - \frac{\delta_{ij}}{3}\tilde{S}_{kk}\right), \tag{5}$$

where $\bar{\Delta}$ and C_S indicate the local grid scale and the unknown model coefficient, respectively, and $\left|\tilde{S}\right| = \left(2\tilde{S}_{ij}\tilde{S}_{ij}\right)^{1/2}$ denotes the magnitude of the resolved strain rate tensor.

$$\tilde{S}_{ij} = \frac{1}{2}\left(\frac{\partial \tilde{u}_i}{\partial x_j} + \frac{\partial \tilde{u}_j}{\partial x_i}\right). \tag{6}$$

In Eq. (5), C_S is determined by the Germano identity by the least-square method [36,38].

2.2. *Validation of unsteady turbulent flow*

The flow around a cylinder is characterized by complex features such as massive separating flow and unsteady wakes [40-42]. To ascertain the accuracy and reliability of our numerical method, we perform a three-dimensional simulation of unsteady turbulent flow over a circular cylinder. Fig. 1(a) shows a schematic of the computational domain. To reduce the effect of the boundary condition, the upstream and downstream far-field boundaries of the flow are approximately 10 and 50 cylinder diameters (D), respectively, away from the cylinder, similar to a previous study [32]. The spanwise length L_z of the circular cylinder is set to $5D$ because the spanwise two-point correlations decreased to nearly zero within the domain [43]. At the inlet, a pressure far-field condition is imposed based on Riemann invariants (i.e., characteristic variables) to model a freestream condition at infinity with a Mach number. The pressure outlet boundary condition is employed at the exit, and a no-slip boundary condition is imposed on the surface of the circular cylinder. A periodic boundary condition is employed in the spanwise direction. The Reynolds number of this numerical simulation is 1.66×10^5 based on the cylinder diameter D and freestream velocity U_∞, and the Mach number is 0.166. In Fig. 1(b), the adopted grid spacing is comparable to that of a previous study of Cheng et al. [42], and the total cell numbers and detailed mesh resolutions are summarized in Table 1. The uniform grid spacing on the circular cylinder surface is applied in the circumferential direction (θ-direction). In the wall-normal direction (r-direction), the mesh is stretched based on a hyperbolic tangent function. The first height of a grid cell in the wall-normal direction is $\Delta r_{wall}^+ \approx 0.8$ to resolve the turbulent boundary layer [42]. The two-dimensional grid shown on the xy plane in Fig. 1(b) is duplicated in the spanwise direction to obtain a three-dimensional grid. The grid spacing in the spanwise direction is uniformly distributed with $\Delta z/D = 2.6 \times 10^{-2}$, comparable to that of previous studies [40-41]. The time step of $\Delta t = 1.0 \times 10^{-5}$ s for the simulation of the circular cylinder is comparable to that of an earlier study of Zhang et al. [10]. The total physical time is approximately 1.5 s, corresponding to $1890D/U_\infty$. The simulation was performed initially for $378D/U_\infty$ to eliminate the transient process, and the temporally averaged flow statistics were calculated over the last $1512D/U_\infty$.

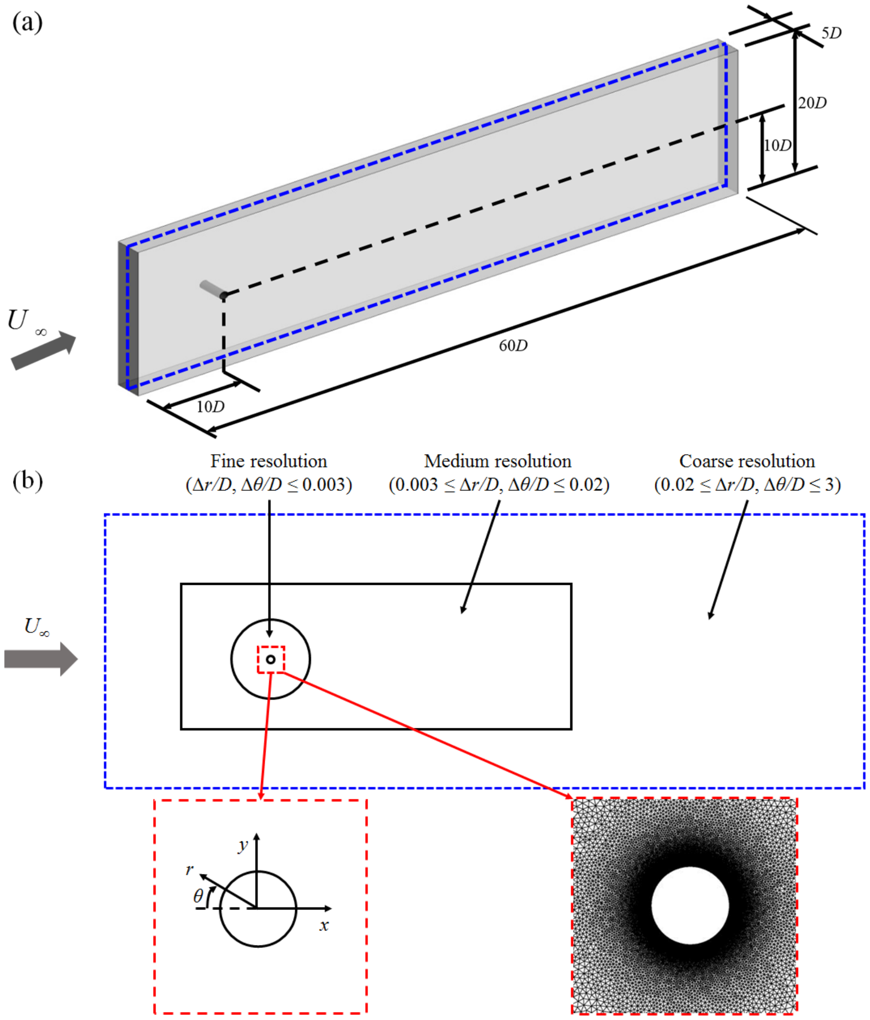

Fig. 1. Schematic of computational domain for an unsteady turbulent flow over a circular cylinder. The circumferential angle θ is measured in a clockwise direction. Three different grid resolutions on the xy plane (blue dashed line at center of spanwise domain in (a)) are highlighted in (b), and a grid resolution topology and a close-up view of the adopted fine grid are illustrated.

Fig. 2 shows the distribution of the pressure coefficient C_p and the Strouhal number peaks St_p as a function of θ for a circular cylinder. Here, the Strouhal number is defined based on the frequency, cylinder diameter D, and freestream velocity U_∞, and the circumferential angle θ starts from the stagnation point in the clockwise direction

(Fig. 1b). In Fig. 2(a), the distribution of C_p from our LES is almost identical to that of the previous experimental data of Jenkins et al. [43], although there is a slight difference on the backward face between θ = 110 and 240º because of the relatively coarse grid resolution in the wake region. The distribution of the Strouhal number peaks is in good agreement with that of Jenkins et al. [43]. This good agreement with the experimental data provides credence to the numerical setup of the present LES method.

Number of cells	Surface grid		$\Delta\theta/D$	$\Delta z/D$	$\Delta r_{min}/D$ (Δr_{min}^{+})
	N_θ	N_z			
46.14 M	504	189	2.7×10^{-4}	2.6×10^{-2}	4.4×10^{-6} (0.8)

Table 1. Numerical details for turbulent unsteady flow past a circular cylinder. θ, r, and z are the coordinates in the circumferential, radial, and spanwise directions, respectively. N_θ and N_z are the number of grid points on the surface in the circumferential and spanwise directions, respectively, and Δr_{min} denotes the minimum resolution in the radial direction.

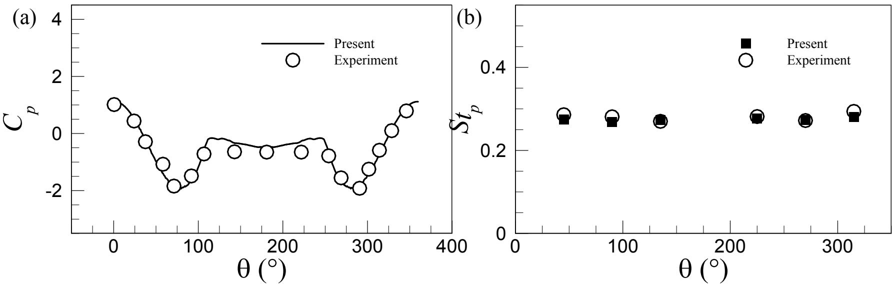

Fig. 2. Distribution of (a) pressure coefficient C_p and (b) Strouhal number peaks St_p as a function of θ for a circular cylinder. Experimental data (open circles) of Jenkins et al. [43] are included for validation.

2.3.Simulations of flows around multi-element iced airfoils

To simulate flows around multi-element iced airfoils, we employ iced airfoil configurations generated under SLD condition and non-SLD condition [18,44]. The flow conditions to determine the ice shapes for the two types of iced airfoils are summarized in Table 2. The ice shape under the SLD condition was obtained by the numerical simulation of Raj et al. [18], and that under the non-SLD airfoil was experimentally made in a facility at the NASA's Glenn's Icing Research Tunnel IRT [44]. A simulation of a clean multi-element airfoil is conducted as a comparison using the McDonnell Douglas Aerospace 30P30N [44,45] as used by many previous studies [18,30-31] because of its high lift. The two iced airfoils are generated using this clean airfoil as a base under the flow conditions listed in Table 2. The configuration of this multi-element clean airfoil with the slat, main, and flap elements is shown in Fig. 3. In the slat element, the slat cusp denotes a sharp point near the leading edge, and a small region near the pressure side indicates a slat cove. Similar to the slat cove, the main element includes a flap cove near the lower trailing edge of the main element. The slat gap Gap_s and the flap gap Gap_f are also shown between the elements. Further detailed information for the clean airfoil (e.g., deflection angle, gap size, and overhang distance) is tabulated in Fig. 3.

Case	LWC (g/m^3)	MVD (μm)	Mach number	AOA (°)	Temperature (K)	Duration (min)
SLD	1.44	154	0.27	16	270.3	15
Non-SLD	0.6	20		8	268.2	6

Table 2. Flow conditions for SLD and non-SLD cases. LWC, MVD, and AOA denote liquid–water content, mean volumetric diameter, and angle of attack, respectively.

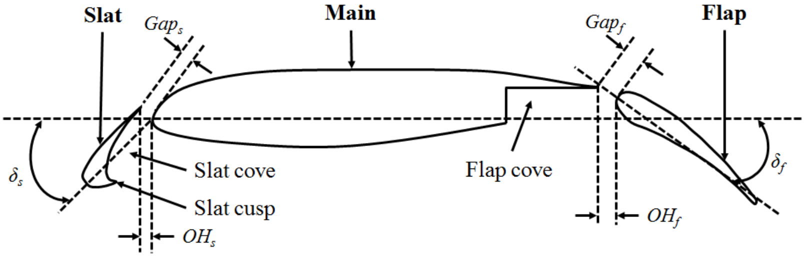

Stowed chord $c = 32$ inch		
Slat element deflection angle	δ_s	30˚
Flap element deflection angle	δ_f	30˚
Slat element gap	Gap_s	2.95%
Flap element gap	Gap_f	1.25%
Slat element overhang	OH_s	2.5%
Flap element overhang	OH_f	0.5%

Fig. 3. Configuration of three-element high-lift clean airfoil.

2.3.1. Ice shapes on multi-element airfoils under SLD and non-SLD conditions

Fig. 4 shows the ice shapes on the slat, main, and flap elements for MVDs of 20 μm (non-SLD condition) and 154 μm (SLD condition). As shown in Fig. 4(a), upwind horn-shaped ice on the suction side near the slat leading edge appears under the non-SLD condition, while a large accretion of ice occurs on the slat element under the SLD condition. Inside the slat element (i.e., pressure surface), ice accretion hardly occurs regardless of the value of the MVD. As shown in Fig. 4(b), at the leading edge of the main element, the non-SLD case displays horn-shaped ice. Under the SLD condition, the icing region on the lower surface of the main element moves downstream (runback ice). At the trailing edge of the main element in Fig. 4(c), a large ice accretion appears under the element for the SLD case but only slightly for the non-SLD case. The ice shape of the SLD case is caused by the large inertia effect of the droplets compared to that of the non-SLD case [15], indicating that small diameter droplets follow the streamline better. For the flap element in Figs. 4(c) and (d), the non-SLD case induces a small ice accretion on the lower surface, while the

SLD case induces a broader icing region (except for the upper surface of the trailing edge), resulting in an ice-covered flap. As shown in Fig. 4(c), the ice shape at the flap leading edge for the SLD case leads to a blocked gap between the main and flap elements.

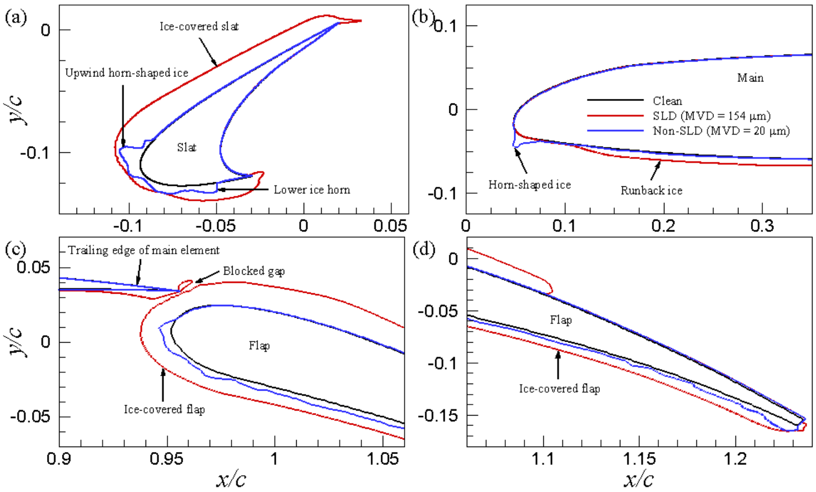

Fig. 4. Comparison of ice shapes on multi-element airfoils under SLD and non-SLD conditions: (a) slat element, (b) leading edge of main element, (c) flap gap, and (d) flap trailing edge.

2.3.2. Computational domain and mesh resolutions

Fig. 5 shows the computational grids for the clean, SLD, and non-SLD airfoil cases. The basic type of grid topology is on O-type hybrid grid. The location of the far-field boundaries is 25 chord lengths (c) away from the airfoils to minimize the effect of the boundary condition, and a no-slip boundary condition is adopted on the surface of the multi-element airfoils for all cases. In the simulations of flows around the multi-element iced airfoils, local coordinates (i.e., ξ and η) are introduced, where ξ and η denote the coordinates along the circumference direction and the wall-normal direction in a local region on each element. Although not shown here, the pressure coefficient with a doubled far-field location had a negligible influence of the domain size for all cases. On the side boundary (i.e., in the spanwise direction), a periodic boundary condition is applied [46-47]. Although a long spanwise domain size ($z/c \geq$

0.1) is required to capture the flow characteristics of the stall and post-stall conditions [48], a LES for a flow over an airfoil (i.e., A-airfoil designed by Aérospatiale) near stall at a high Reynolds number (2.1×10^6) based on the chord length and freestream velocity of Mary and Sagaut [46] showed that the mean and fluctuating velocity with a small spanwise extent of 0.005–0.03 *c* are in good agreement with previous experimental data [49]. Furthermore, You and Bromby [50] found that the pressure distribution on the surface of a Sikorsky SSC-A09 airfoil estimated using a LES with a small spanwise domain ($z/c = 0.04$) agrees well with previous experimental data [51] even at an AOA of 14°. Because the flow conditions (i.e., Reynolds number and Mach number) employed in the present study are comparable to those of the previous numerical study of You and Bromby [50], a spanwise domain size of 0.04 *c* is used in this study. Although not shown here, this domain size was confirmed based on the convergence of the spanwise correlation to zero at less than half of this domain size.

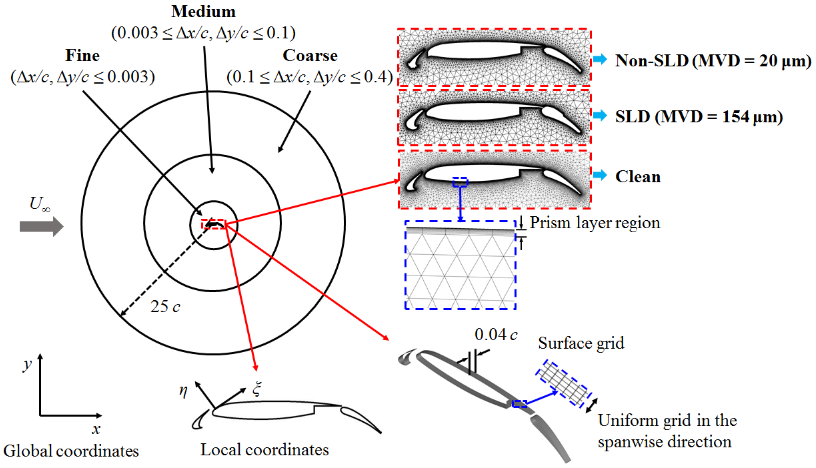

Fig. 5. Computational domain and grids around multi-element airfoils (*c* denotes the stowed chord length).

As shown in Fig. 5, we employ three different grid resolutions, i.e., fine, medium, and coarse, through the entire domain (black solid lines). Near the no-slip surface, 16 prism layers are imposed to accurately capture flows near the wall. A non-uniform grid is adopted in the wall-normal direction (η-direction) based on a hyperbolic tangent function within the prism layers. Except for the prism layers, an unstructured mesh is applied on the *xy* plane for all simulations. A three-dimensional grid is adopted by duplicating the two-dimensional grid configuration on the *xy* plane uniformly in the spanwise direction. The surface grid details are given in Table 3. A grid sensitivity test using grid resolutions of 15.71 million (coarse grid), 22.02 million (base grid), and 27.14 million (fine grid) cells confirmed that the pressure coefficients C_p for the medium and fine grids are almost identical (not shown here).

Case	Number of grid points N_ξ			Number of cells on *xy* plane	Total number of cells
	Slat	Main	Flap		
Clean	1,165	2,753	500	218,011	22.02 M
SLD	1,500	4,500	1,500	197,059	37.24 M
Non-SLD	1,628	2,174	1,024	141,597	26.76 M

Table 3. Computational grid details. N_ξ denotes the number of grid points along the airfoil surface on the *xy* plane.

Fig. 6 shows the distribution of the grid sizes on the surface along the circumferential direction ($\Delta\xi_{wall}^+$), the first grid height on the surface ($\Delta\eta_{wall}^+$) and the time step sizes in wall units (Δt^+) according to the LESs of flows over the clean, SLD, and non-SLD cases at an AOA of 8° for brevity. In Fig. 6(a), the mesh resolutions of all cases in the circumferential direction are less than 40 wall units except for a narrow region near the main leading edge of the clean case [52-53]. When the first grid sizes on the surface are $\Delta\eta_{wall}/c = 5.635 \times 10^{-6}$ and 3.565×10^{-6} for the clean and iced airfoils, respectively, Fig 6(b) shows that the values of maximum $\Delta\eta_{wall}^+$ are less than 0.8 throughout the airfoil elements. For all cases, large values of $\Delta\eta_{wall}^+$ are observed at the trailing edges of the slat ($x/c \approx 0.02$) and main ($x/c \approx 0.95$) elements because of the flows around the bluff shape. At the other AOA (not shown), the values of $\Delta\xi_{wall}^+$ and $\Delta\eta_{wall}^+$ for all cases are less than 48 and 0.8, respectively. In the spanwise direction, the grid resolutions are $\Delta z/c = 2.191 \times 10^{-4}$ and $\Delta z/c = 1.925 \times 10^{-4}$ for the clean and iced airfoils, respectively, leading to $\Delta z_{wall}^{+} \leq 40$, except for only a few grid points ($\Delta z_{wall}^{+} \approx 48$). Although not shown here, a grid test using a finer spanwise grid resolution ($\Delta z_{wall}^{+} \approx 24$) indicates that the influence of the mesh resolution is small.

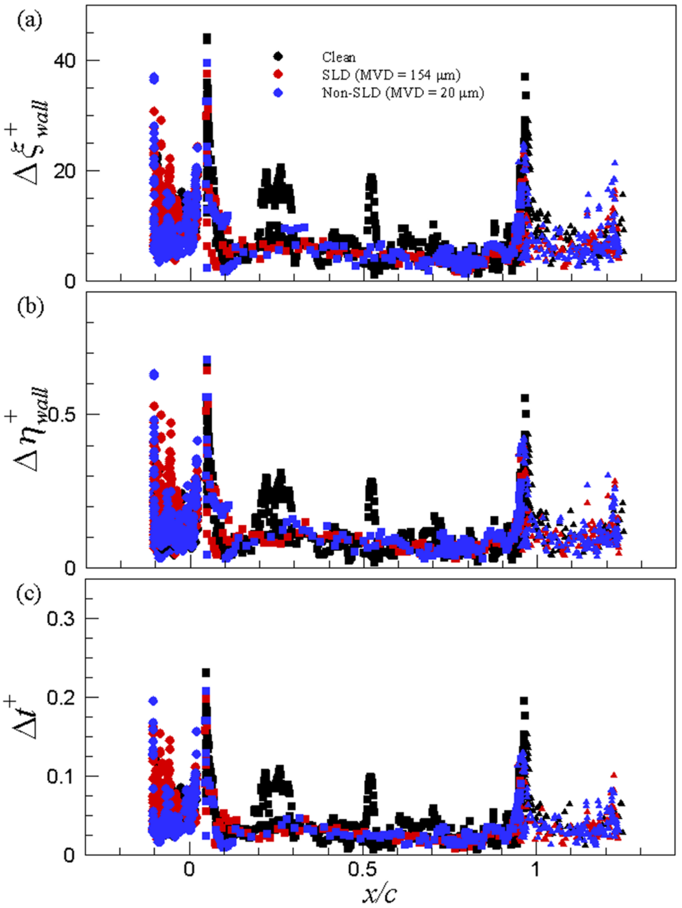

Fig. 6. Distribution of (a) grid sizes on the surface along the circumferential direction, (b) first wall-normal height of grid cells along the chordwise direction, and (c) time step sizes. Circles, rectangles, and triangles denote data on the slat, main, and flap elements, respectively.

The time step of all cases is $\Delta t = 1.0 \times 10^{-6}$ s, corresponding to the non-dimensional time steps ($\Delta t^{*} = \Delta t U_{\infty}/c$) of 9.68×10^{-5} and 1.58×10^{-4} for the two types of iced airfoils and the clean airfoil, respectively. The time step yields a maximum acoustic Courant-Friedrichs-Levy (CFL) number for all cases less than 10, comparable to that of a previous study of Asada and Kawai [54]. Furthermore, Fig. 6(c) clearly shows that the present temporal resolutions are sufficient for all cases to satisfy a criterion of $\Delta t^+ \leq 0.4$ by Choi and Moin [55] for capturing accurately the near-wall turbulence. The Reynolds number of all cases is 4.9 million based on the freestream velocity U_∞ and chord length. The Mach number Ma and temperature T are 0.27 and 268.2 K, respectively. The total time period is approximately $87c/U_\infty$, corresponding to a physical time step of approximately 0.9 s. The first sampled data for $38c/U_\infty$ was discarded to remove the transient effects, and statistics were collected over the last $49c/U_\infty$.

3. Results and discussion

3.1. Mean properties

In this section, turbulent statistics such as lift coefficient, ratio of lift to drag, surface pressure coefficient, mean velocity with streamlines, and Reynolds stresses are examined with varying AOAs. The LES results are compared with independently simulated URANS data to show the prediction improvement of our LES data for multi-element airfoils. For the two-dimensional URANS simulations, the total number of grids used are 0.16 million, 0.19 million, and 0.14 million for the clean, SLD and non-SLD cases, respectively. To compute the eddy viscosity, the shear–stress transport (SST) turbulence model proposed by Menter [56] is used. The first points off the wall $\Delta\eta_{wall}^+$ are less than 1.0 to resolve the turbulent boundary layer. The numerical details for the URANS simulation are identical to those of the current LES, except for the filtered NS equations with the dynamic Smagorinsky model. To obtain the initial flow fields for the URANS simulations, a steady RANS computation is performed until residuals of less than 3 orders of the velocity magnitude are obtained. The steady RANS solution is then applied as the initial condition for the URANS computations. The URANS computations were performed for 0.04 s corresponding to non-dimensional times of tU_∞/c = 5.64 and 3.45 for the clean and iced airfoils, respectively, to eliminate the transient effect. The URANS data were then collected at intervals of 2×10^{-6} s ($\Delta tU_\infty/c = 3.17 \times 10^{-4}$ and 1.94×10^{-4} for the clean and iced airfoils, respectively), and the sampling time duration was 0.04 s.

3.1.1. Lift and drag coefficients

The mean lift coefficient as a function of the AOA at AOAs of 0, 4, 8, 12, and 16º are shown in Fig. 7. The experimental data [45] of the lift coefficient for a clean airfoil is included to further validate the simulations. In Fig. 7, the LES results (thick black lines) show that the lift coefficients of the clean airfoil for all elements (i.e., slat, main, and flap elements) match well with those of the experimental data regardless of the AOA. However, the URANS approach (thin red lines) shows a poor prediction of the lift coefficients for all elements, and the differences between the URANS and experimental data of each element gradually increase with an increase in the AOA, consistent with earlier observations for steady RANS results of single-element iced airfoils [9-11,22]. The lift coefficients of the slat and main elements (Figs. 7a-b) from the URANS simulation for the clean and iced airfoils are greater than those of the LES at all AOAs. In contrast, the flap lift coefficients (Fig. 7c) of the URANS simulation for the clean airfoil are smaller than those of the LES data regardless of the AOA.

As shown in Fig. 7, the LES data show that the ice accretions over the main and flap elements lead to a significant degradation of the lift coefficients for both the SLD and non-SLD cases regardless of the AOA. However, the change in the slat lift coefficients is relatively small compared to that of the clean airfoil because of the relatively small size of the slat element. However, it should be noted that the ice shape on the slat element is a dominant contributor to the aerodynamic penalties because flows near the slat element interact with the flows developed by the other elements. The LES results reveal that the main element accounts for more than 80% of the total reduction of the lift coefficient because of the overwhelming size of the main element compared to that of the other elements (Fig. 4). Compared to the clean airfoil, the maximum total lift loss in the SLD and non-SLD cases are approximately 40% and 30%, respectively. The lift loss of the SLD case is similar to that of a single-element iced airfoil [12] because the large ice accumulation on both the slat trailing edge and flap leading edge for the SLD case (Fig. 4) results in clogging within the slat and flap gaps. The larger lift loss under the SLD condition compared to that under the non-SLD condition suggests that the lift loss is significantly influenced by the icing condition, in particular by the droplet size, consistent with previous findings for both single- and multi-element iced airfoils [1,15,18]. However, it should be noted that although the droplet size is sufficiently large (MVD = 400 μm), the short freezing time to construct the ice accretion can lead to a large slat and/or flap gap, reducing the lift loss [57]. The lower lift loss of the non-SLD case compared to than that of the SLD case is contrary to an earlier observation from steady RANS simulations [18]. The difference in the lift loss between the present and previous data is mainly due to large ice accretion on the suction side of the main element under the non-SLD condition after a long freezing period.

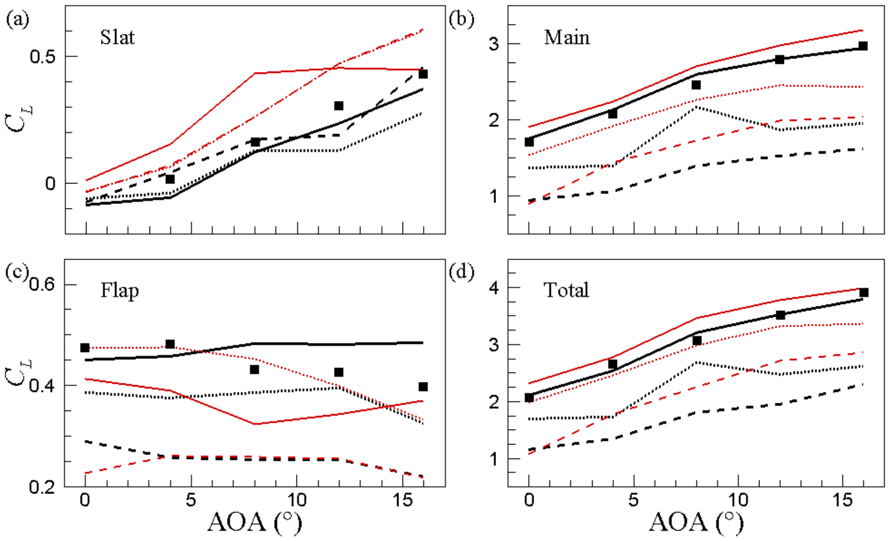

Fig. 7 Profiles of lift coefficient as a function of AOA. Solid, dashed, and dotted lines indicate data of clean, SLD, and non-SLD cases, respectively. Thick black and thin red lines denote the LES and URANS data, respectively. For comparison, the experimental data of Valarezo et al. [45] are included in each figure (closed rectangles).

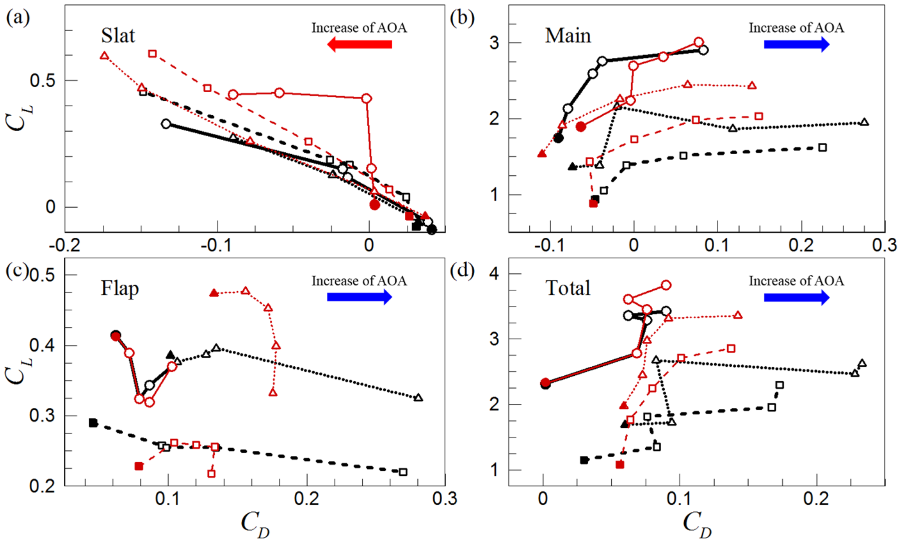

Fig. 8 Profiles of the ratio of lift to drag. The lines are identical to those in Fig. 7. Circles, rectangles, and triangles denote data of clean, SLD, and non-SLD cases at AOAs of 0, 4, 8, 12, and 16° (thick black lines (LES) and thin red lines (URANS)). The data at an AOA of 0° are depicted by closed symbols to indicate the start of the variation with respect to the AOA of each airfoil element.

Fig. 8 shows the variations of lift coefficients as a function of the drag coefficients for the clean, SLD and non-SLD cases. It is clear that the ice accretions on the multi-element airfoils lead to a significantly increased total drag at all AOAs, consistent with the previous observations of Khodadoust et al. [31] for a multi-element iced airfoil. The ice shapes for the two types of iced airfoils resulted in an increased drag for the main and flap elements, and this result differs with that of the slat element because of the recirculating flow (or SB) within the slat cove. The total amount of increased drag owing to ice accretions is mostly induced by the drag on the main element, similar to the lift loss on the main element. A larger total drag is observed on the main element of the non-SLD case compared to the SLD case because the horn-shaped ice on the lower surface of the main element (Fig. 4) leads to a significantly increased drag similar to that of the finding by Raj et al. [18]. Compared to the LES approach, the URANS method predicts small drag coefficients on the main and flap elements at an AOA greater than 8°. The difference in the slat drag coefficients between the URANS and LES data is relatively small for the SLD case. The large difference for the non-SLD case can be attributed to the incorrectly predicted flow features near the upwind horn-shaped ice on the slat element by the URANS method (shown later).

3.1.2. Surface pressure coefficient

Figs. 9-11 show the variations of the mean pressure coefficient C_p along the chordwise direction for the clean, SLD, and non-SLD cases at AOAs of 0, 4, 8, 12, and 16º. Previous experimental data [14] of C_p for a clean airfoil is included to provide a reliability of the present simulation. The values of C_p for the clean airfoil predicted by the LES (closed circles) are in good agreement with the experimental data (open circles) at AOAs of 4, 8, and 16º. Compared to the LES data, the suction peaks predicted by the URANS simulation (diamond symbols) near the slat element are generally great for all cases, and the difference is significant at higher AOAs. In particular, C_p of the URANS simulation for the non-SLD case (blue diamond) has significantly higher values on the suction side of the slat element compared to those of the LES (blue circle) in Fig. 9. On the main and flap elements (Figs. 10-11), the URANS method predicts higher suction peaks near the leading edges than the LES for the clean and non-SLD cases. However, the SLD case shows similar values between the LES and URANS for the two elements. The increased C_p near the leading edge of the flap element of the clean case is opposite to the decreased lift coefficient (Fig. 7c) because the pressure level on the suction side near the flap trailing edge from the URANS simulations decreases rapidly.

In Fig. 9, the LES data show that the ice accretions on the slat elements of the two iced airfoils act as a leading-edge extension (from x/c = -0.094 to -0.106) (see Fig. 9e). In addition, the pressure on the suction side of the slat element (red and blue circles) is significantly higher than that of the clean airfoil (black circles) at AOAs of 0 to 12º, consistent with the increase in the lift on the slat element in Fig. 7(a). However, the values of C_p near the slat leading edge (x/c = -0.105) are low compared to those of the clean airfoil at an AOA of 16º. The peaks near the slat trailing edge of the SLD case (red circle) increase significantly compared to the clean airfoil (black circle) at all AOAs because the presence of an increased surface curvature by the ice shape near the slat trailing edge (Fig. 4a) leads to accelerated flows. For the non-SLD case (blue circle), the peak near the slat trailing edge ($x/c \approx 0.01$) is slightly greater than that of the clean airfoil up to an AOA of 8º, whereas it is smaller at AOAs ≥ 12º, especially at an AOA of 16º (Fig. 9e) as SBs emerged on the suction side of the slat element (shown later).

On the main element (Fig. 10), strong suction peaks near the leading edge of the clean airfoil are evident, and the magnitude of the peaks increases with an increase in the AOA. However, the suction peaks for the two iced airfoils decrease compared to the clean airfoil, and the magnitude variation of the peaks is not significant as the AOA increases. Because the capability to maintain high suction peaks is directly associated with the generation of high lift [31], the reduced suction peaks for the iced airfoils are consistent with the degradation of the lift coefficients by the main element (see Fig. 7b). On the upper surface of the main element for the non-SLD case at an AOA ≥ 8º (see Figs. 10c–e), the pressure recovery process is observed with flow separation, transition, and reattachment. On the flap element, the suction peaks at the leading edge of both the SLD and non-SLD cases are smaller than those of the clean airfoil at an AOA ≥ 4º because of the ice accretion near the gaps. At an AOA of 0º, the higher suction peak for the non-SLD case compared to that of the clean airfoil is attributed to a delayed flow separation on the flap element (shown later). It should be noted that the smallest suction peaks on the main and flap elements are observed for the SLD case at all AOAs compared to those of the clean and non-SLD cases due to the reduced slat- and flap-gap distances caused by the ice accretions (Figs. 4a and c), resulting in a large lift loss for the main and flap elements (Figs. 7b and c).

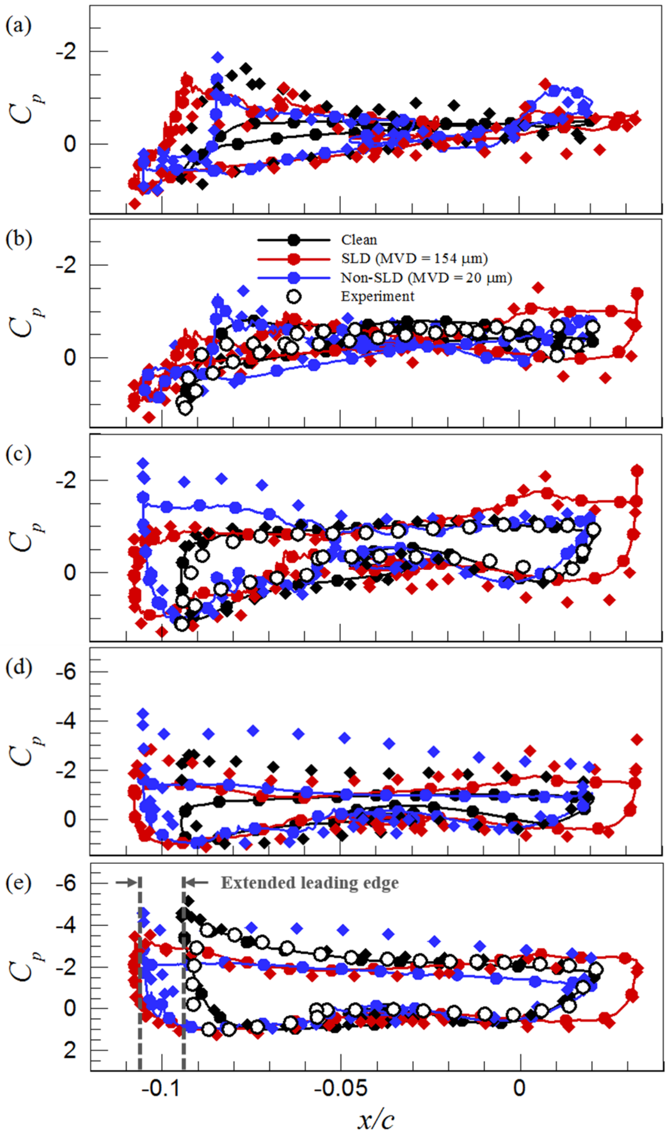

Fig. 9. Pressure coefficient C_p on the surface of slat elements: (a) AOA = 0º, (b) 4º, (c) 8º, (d) 12º, and (e) 16º. Closed diamonds with colors identical to those of the clean, SLD, and non-SLD cases indicate the data predicted by independent URANS simulations.

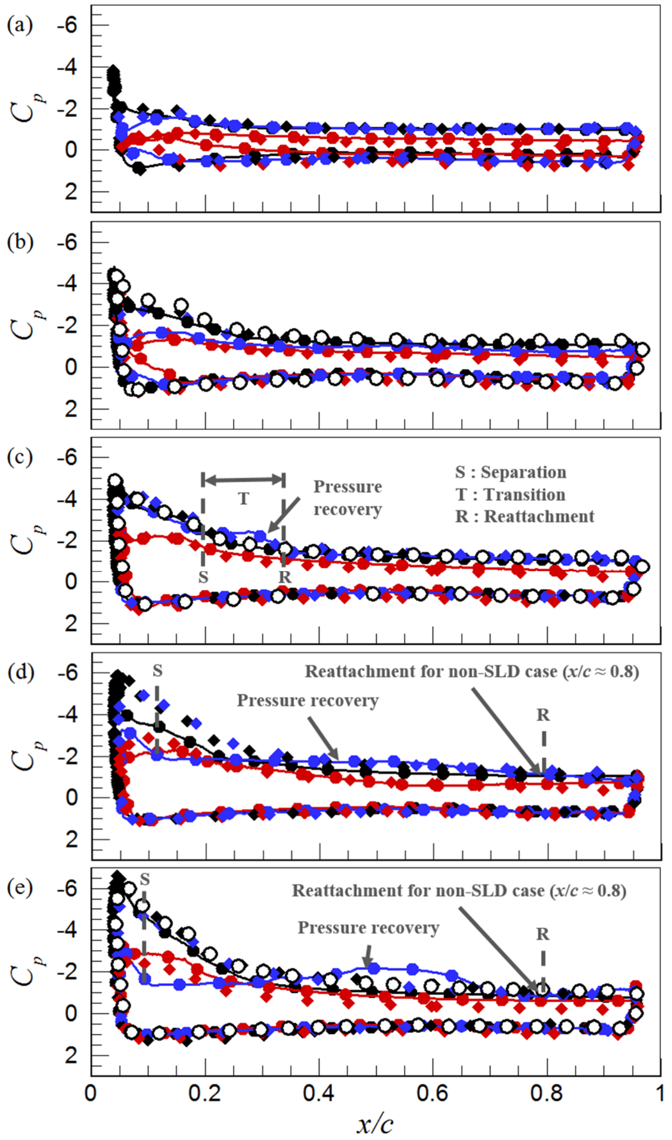

Fig. 10. Identical to those in Fig. 9, but for main elements.

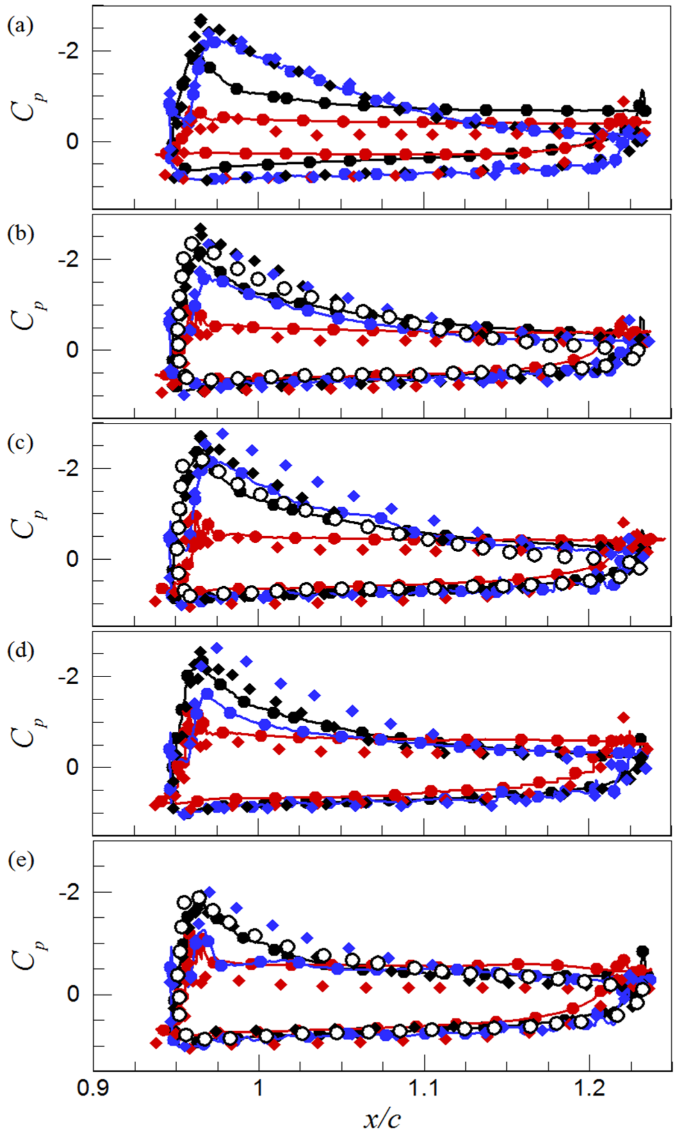

Fig. 11. Identical to those in Fig. 9, but for flap elements.

3.1.3. Mean velocity and streamline

The temporally averaged streamlines and velocity magnitude contours of flow patterns over multi-element airfoils at AOAs of 0, 4, 8, 12, and 16º are shown in Figs.

12–14. The temporally averaged velocity magnitude is defined as $U_{mag} = \left\langle \sqrt{\overline{u}^2 + \overline{v}^2 + \overline{w}^2} \right\rangle$. In Fig. 12, a comparison of the predicted velocity contours between the LES and URANS data shows that the velocity magnitude obtained by the URANS simulation for the clean airfoil is greater than that by the LES at all AOAs (see contour levels) because the stagnation points predicted by the URANS method are located further downstream on the slat and main elements (see values of x_{stag}/c). The further downstream positions of the stagnation points of the URANS method accelerate the flow over the slat and main elements, and lead to an increase in the lift and suction peaks (Figs. 7a-b, 9, and 10). Nevertheless, the stagnation positions on the flap element for the two methods are identical regardless of the AOA. In contrast to the LES data, a secondary SB within the slat cove is observed in the URANS data up to an AOA of 12° (see red dashed lines in enlarged view of URANS data). In addition, the size of the primary SBs within the slat and flap coves from the URANS data is slightly smaller than that of the LES at an AOA ≥ 4° (see inset in Figs. 12c–j). The smaller SBs from the URANS simulations lead to a flattened trajectory of shear layers (SLs) generated from the slat cusp and flap cove lip (see Fig. 12d). As a result, the increased mass flow through the slat and flap gaps creates high suction peaks on the main and flap elements (Figs. 10-11). Compared to the LES, flow separations on the main element are not observed at all AOAs for the URANS data (see values of $x_{sep/c}$) resulting in an increased lift on the main element (Fig. 7b).

As the AOA increases, the LES data show that the mass flow rate increases through the slat gap with a reduction of the primary SB in size, leading to increased suction peaks (Fig. 10). The flow separations on the main element are continuously delayed up to an AOA of 12°. However, a separation point at an AOA of 16° occurs further upstream compared to that at an AOA of 12°. On the flap element, the positions for the flow separations are not sensitive to the variation of the AOA in the range 4–8°. However, the flow separations are accelerated with an increase in the AOA (≥ 12°).

The streamlines predicted by both LES and URANS for the SLD case in Fig. 13 show primary SBs in the slat and flap cove regions for all AOAs similar to the flows over the clean airfoil (Fig. 12). However, because the slat and flap gaps decrease because of ice accretion (see Figs. 4a and c), these primary SBs are significantly greater than those of the clean case at all AOAs. The narrowed slat and flap gaps result in decelerated flows over the elements at all AOA compared to the clean airfoil (see contour levels), reducing the suction peaks on the main and flap elements of the iced airfoil (Figs. 10-11). The decreased flap gap leads to a flap unloading as shown in Fig. 7c, suggesting that the ice accumulation near the flap gap causes a more significant flap unloading than that of the wakes generated by the slat and main elements. Compared to the clean airfoil, flow separations on the main element are delayed at all AOAs, whereas early separations are found on the flap element with little variation as the AOA increases. A comparison of the data between the LES and URANS methods for the SLD case shows that the overall difference in the stagnation points, separation points, and size of primary SBs within the slat and flap coves is similar to that of the clean airfoil (Fig. 12). However, the stagnation points predicted by the LES are located further downstream on the main element at an AOA ≤ 4° compared to the URANS data because of the effect of a stretched SB shed from the slat leading edge (see Figs. 13c–d).

For the non-SLD case shown in Fig. 14, both the LES and URANS results show primary SBs within the slat and flap coves regardless of the AOA. In addition, they both predict secondary SBs aft of the upwind horn-shaped ice for all AOAs (red dashed lines), although the URANS method gives rapidly increased SBs on the upper surface of the slat element as the AOA increases compared to the LES approach. Contrary to the LES prediction, secondary SBs within the slat cove are found using the URANS method at an AOA ≥ 8° (red dashed lines in Figs. 14f, h, and j), similar to those of the clean airfoil (Fig. 12). Furthermore, the URANS approach does not resolve a primary SB found on the main element at an AOA ≥ 8° by the LES method (orange line for mean stagnation line).

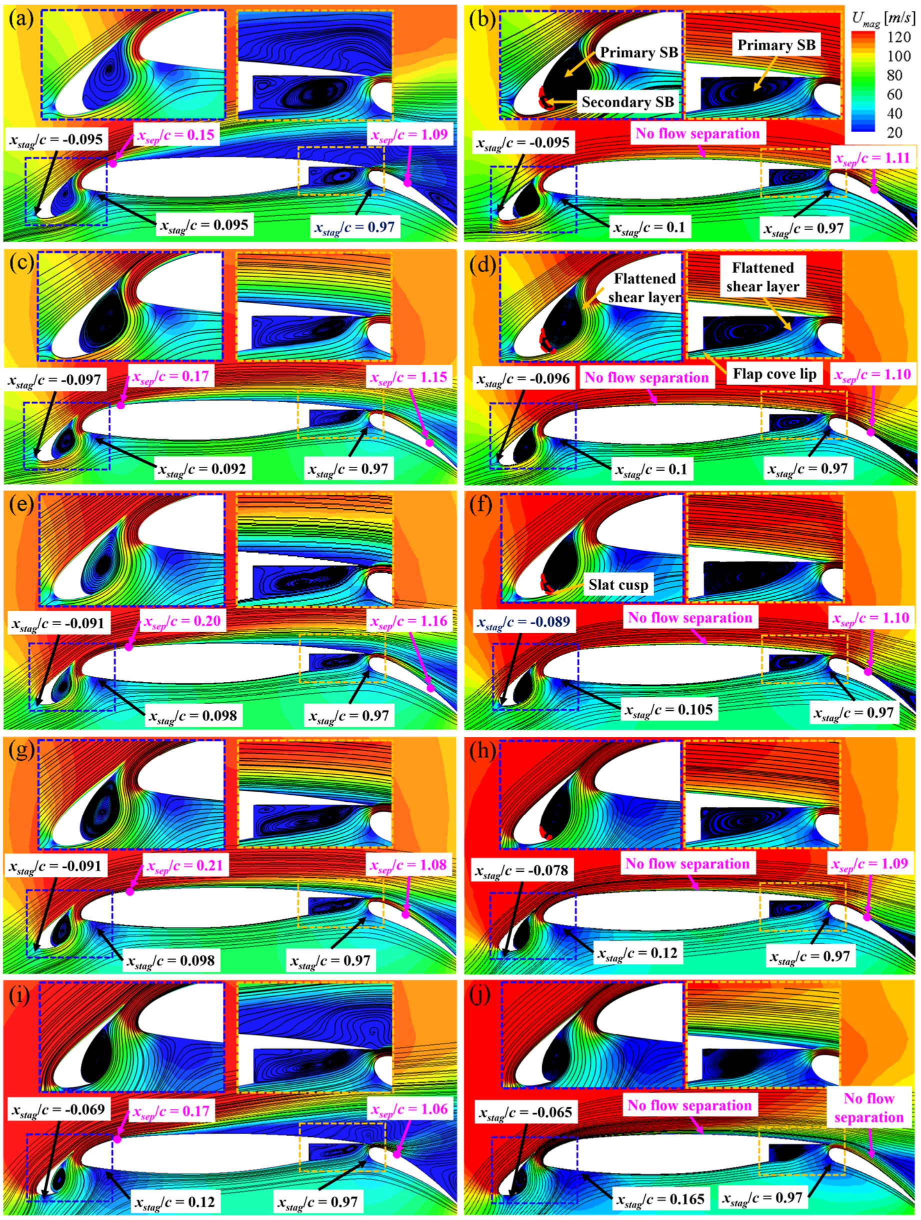

Fig. 12 Temporally averaged streamlines with velocity magnitude for clean airfoil: (a, b) AOA = 0º, (c, d) 4º, (e, f) 8º, (g, h) 12º, and (i, j) 16º. The left and right figures denote the LES and URANS data, respectively. Red dashed lines within the slat cove on URANS data (enlarged view) indicate a SB.

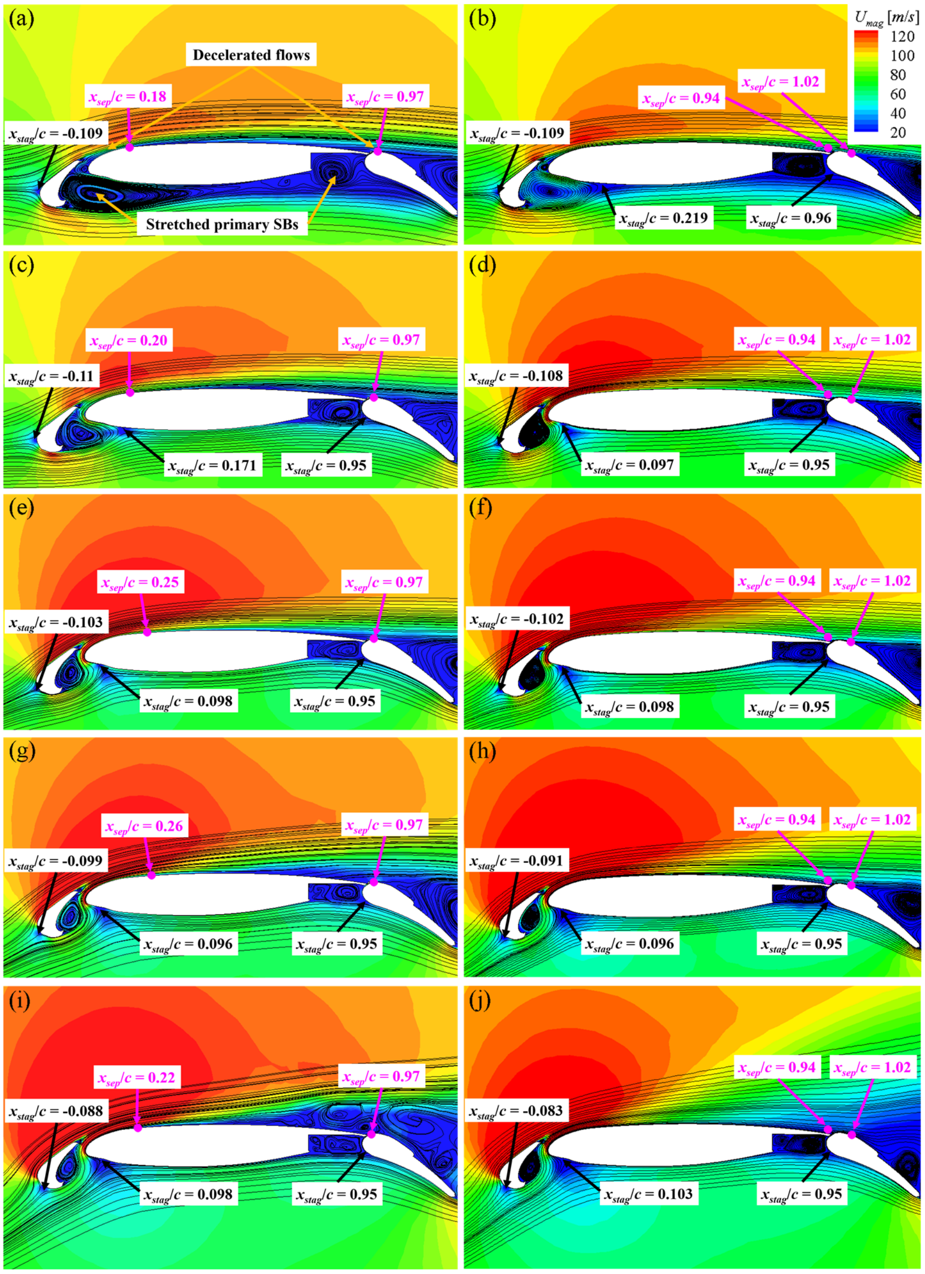

Fig. 13 Identical to those in Fig. 12, but for SLD case.

Fig. 14 Identical to those in Fig. 12, but for non-SLD case. Solid orange lines denote the mean stagnation lines generated by primary and secondary SBs on upper surfaces of slat and main elements.

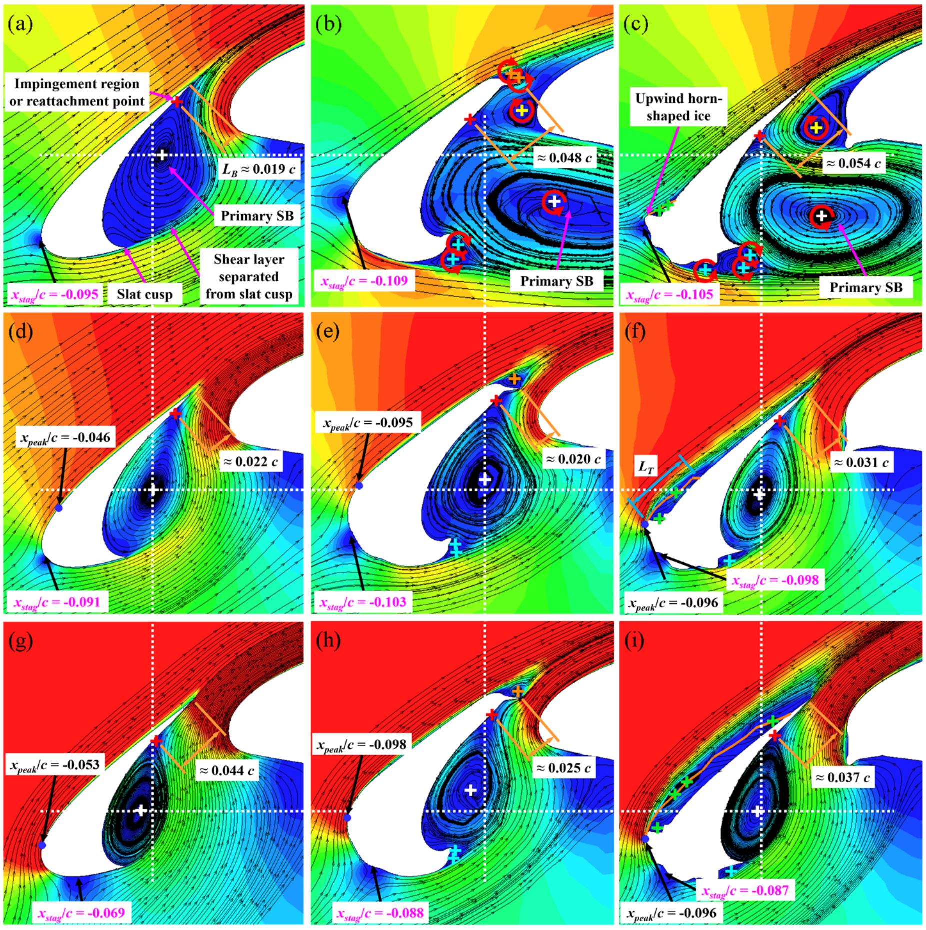

Fig. 15 Temporally averaged streamlines with velocity magnitude around slat element for clean (left), SLD (middle), and non-SLD (right) cases: (a, b, c) AOA = 0º, (d, e, f) 8º, and (g, h, i) 16º. The contour level colors are identical to those in Fig. 12. White and red crosses indicate the centers of SBs within the slat cove and near the reattachment points, respectively. Sky-blue, orange, and yellow crosses denote the centers of SBs near the slat leading edge (or cusp), slat trailing edge, and main leading edge, respectively. For the non-SLD case (right), solid orange lines denote the mean stagnation lines on the upper surface of the slat element. Green crosses represent the centers of SBs aft of the upwind horn-shaped ice on the upper surface of the slat element. White vertical and horizontal dashed lines depict the center location of a primary SB within the slat cove at an AOA of 8º for the clean airfoil to highlight the change of the SB centers with respect to the AOA and airfoil type, respectively. Red arrows indicate the rotational direction of SBs, and x_{peak} indicates locations at which maximum suction peaks occur.

As shown in the pressure coefficient distribution (Fig. 10), this primary SB plays an essential role in determining the flow pressure recovery process. After the flow separation (‘S’ in Figs. 10c–e), an amplified disturbance by inflection instability (K-H instability) within the primary SB increases the momentum near the wall (i.e., transition), and the separated flow reattaches to the surface of the main element ('R' in Figs. 10c–e) [58]. As the AOA increases, the primary SB on the main element extends rapidly along the streamwise direction, and the center of the primary SB on the main element moves gradually away from the surface. Because the SB is related to a large wake region over the main element, an early flow separation for the non-SLD case is found at $x_{sep}/c \approx 0.97$ at an AOA of 16° on the flap element compared to that of the clean airfoil at $x_{sep}/c \approx 1.06$. In addition to the primary SB, a secondary SB occurs on the upper surface of the main element as the center of the primary SB moves further away from the wall at an AOA of 16°, and this secondary SB has a streamwise length (b_2) of approximately 0.25 c as shown in Fig. 14(i). Although the secondary SB on the main element is relatively small compared to the primary SB, that is located very close to the wall with highly unsteady characteristics. This result implies that this secondary SB is closely related to the unsteady aerodynamic performance of the non-SLD case. On the main and flap elements, flow separations for the non-SLD case at AOAs of 0 and 4° are delayed compared to those of the clean and SLD cases. However, as the AOA increases, early separations are observed on the main and flap elements compared to the clean airfoil case. The difference in the stagnation and separation points between the LES and URANS data is similar to that of the SLD case.

Because flows around a slat element have unique flow characteristics (e.g., SL, SB, and reattachment) [18,59], enlarged velocity magnitude contours with the streamlines around the slat element of the clean and iced airfoils are shown with various AOAs in Fig. 15. The mean velocity contours with the streamlines predicted by the LES are shown only for brevity. In addition, because previous studies have devoted little attention to the SB–SB interactions of multi-element iced airfoils, we focus on these interactions for both the SLD and non-SLD cases. As shown in Fig. 15, the shape and size of a primary SB within the slat cove are significantly affected by the AOA for the clean airfoil. The impingement region (red cross) of a SL shed from the slat cusp within the slat cove moves away from the trailing edge toward the middle of the slat element as the AOA increases. As a result, the distance L_B between the reattachment point and the slat trailing edge increases with an increase in the AOA (i.e., a smaller primary SB within the slat cove at a higher AOA with an increase in L_B), consistent with the observations of Jenkins et al. [59]. In addition, the largest SB with an L_B of 0.011 c inside the slat cove for the clean airfoil is found at an AOA of 4° instead of 0°. The center of the primary SB gradually moves closer to the slat element as the AOA increases (see the variation in the white crosses).

Compared to the clean airfoil, a large primary SB with a longer L_B is observed inside the slat cove at an AOA of 0° for the two iced airfoils, as the primary SB within the slat cove is stretched in the streamwise direction because of the induction of a secondary SB near the leading edge of the main element (see yellow crosses in Figs. 15b and c). The large ice accretion on the upper surface of the slat element for the SLD case shown in Fig. 4(a) leads to a more accelerated flow in the upstream of the slat cusp compared to that of the non-SLD case (see the contour levels in Fig. 15). The stretching of the primary SB is significant for the SLD case, indicating a large reduction in the mass flow rate through the slat gap with an accompanying large lift loss. Furthermore, the secondary SB on the main element induces a downward shift of the primary SB for both the SLD and non-SLD cases, although it disappears as the AOA increases. The absence of a secondary SB at a high AOA indicates that the center of the primary SB moves to the middle of the slat element, consistent with our observation for the clean airfoil (white dashed lines across the figures). In addition to the secondary SB near the main leading edge, secondary SBs residing near the slat leading and trailing edges (sky-blue and orange crosses) contribute to a significant change in the trajectory of a primary SL shed from the slat leading edge (or cusp) at an AOA of 0°. In particular, for the SLD case (see rotational direction of SBs with red arrows in Figs. 15b and c), the mass flow rate through the slat gap (see velocity contours through the slat gap) is reduced. The decelerated flow decreases the suction peak near the main element, although the suppression of the secondary SB near the leading edge of the main element with an increase of the AOA leads to a slight increase in the suction peak (Fig. 10). The smallest L_B for both the SLD and non-SLD cases is observed at an AOA of 8° (Figs. 15e and f), compared to the AOA of 4° for the clean case. Near the slat leading edge, the ice accretion on the slat element moves the stagnation points for both the SLD and non-SLD cases further upstream than that of the clean case (see values of x_{stag}/c) regardless of the AOA. When the AOA is in the range 4–12º, the surface curvature near the stagnation points is large for the iced airfoils compared to that of the clean airfoil (see surface curvature at AOA of 8º in Fig. 15), resulting in higher pressure coefficients for the iced airfoils (Fig. 9). However, because the large surface curvature near the stagnation points at an AOA of 16º for the clean airfoil leads to an accelerated flow near the slat leading edge, the values of C_p decrease for the iced airfoils compared to that of the clean airfoil (see values of x_{peak}/c for maximum suction peaks in Fig. 15).

The mean stagnation lines on the upper surface of the slat element (orange solid lines) highlight the SBs for the non-SLD case regardless of the AOA. As the AOA increases, the mean stagnation lines grow rapidly because of the generation of other SBs combined with the streamwise stretching (green crosses in Fig. 15i). The growth of the mean stagnation lines with an increase in the AOA can be estimated using the reattachment length L_T/c, where L_T denotes the distance between the upwind horn-shaped ice and the reattachment point on the upper surface of the slat element (see Fig. 15f). Marongiu et al. [60] reported that the reattachment length of a single-element iced airfoil with a horn-shaped ice is proportional to the square of the AOA. Xiao et al. [11] fitted their computed results for a single-element iced airfoil to a curve using the quadratic equation $L_T/c = A\alpha^2 + B$, where α is the AOA in radians, and the values of A and B are 22.38 and 0.0834, respectively. They showed that the reattachment length is expressed by the curve, although there were small discrepancies compared to the wall-modeled LES data ($\Delta L_T/c \approx$ -0.015, 0.028, and -0.012 at AOAs of 3.0, 5.2, and 7.0º, respectively). The procedure of Xiao et al. [11] for a single-element iced airfoil is used to determine the size of the SBs and to confirm the relation between the reattachment length and the AOA. The reattachment length for the multi-element iced airfoil under the non-SLD condition is curve-fitted using the quadratic equation $L_T/c = C\alpha^2 + D\alpha + E$. In the present study, the values of C, D, and E are estimated to as 1.717, -0.195, and 0.021, respectively. These different coefficients (C, D, and E) with the quadratic equation by Xiao et al. [11] are stemmed from the effects of the slat deflection angle (δ_s) (Fig. 3) and ice shapes of the non-SLD case. Table 4 shows that the fitted quadratic equation predicts well the reattachment lengths compared to the computed results. This result suggests that the reattachment length after the upwind horn-shaped ice grows proportionally to the square of the AOA around the multi-element iced airfoil.

Case	AOA (°)				
	0	4	8	12	16
Computed results (L_T/c)	0.019	0.017	0.037	0.041	0.106
Quadratic fitting (L_T/c)	0.021	0.016	0.027	0.055	0.100
Error ($\Delta L_T/c$)	0.002	-0.001	-0.010	0.014	-0.006

Table 4. Reattachment lengths from computed results and quadratic fitting for non-SLD case.

3.1.4. Reynolds stresses

The contours of the streamwise and crosswise Reynolds normal stresses for the clean, SLD, and non-SLD cases at AOAs of 0, 4, 8, 12, and 16° are shown in Figs. 16–18; only the Reynolds stresses predicted by the LES method are shown for brevity. For the clean airfoil (Fig. 16), small streamwise Reynolds stresses are observed around the slat element at low AOAs. However, the stresses gradually increase on the upper surface of the slat element close to the surface (see inset) as the AOA increases because of the wakes from the slat leading edge. For the crosswise component, the Reynolds stresses are large on the pressure side of the slat element at all AOAs (see inset). These results indicate that the crosswise Reynolds stress is a main contributor to the increased turbulent kinetic energy within the slat cove, similar to previous studies of multi-element clean airfoils [47,59].

At an AOA of 0°, a large crosswise Reynolds stress is observed along a separated SL from the slat cusp (see inset of Fig. 16b) but disappears when the AOA is greater than 0° because of the reduced size of the primary SB in the slat cove (Fig. 15). Furthermore, a large crosswise Reynolds stress exists near the secondary separation region within the slat cove at all AOAs and around the impingement region by the SL from the slat cusp up to an AOA of 12° (see insets of Figs. 16b, d, f, and h). The largest crosswise Reynolds stress is observed near the slat trailing edge at an AOA of 4° (Fig. 16d) because the SL from the slat cusp directly approaches the impingement region, thus indicating the smallest L_B (Fig. 15). The magnitude of the Reynolds crosswise stress within the slat cove is very low at an AOA of 16° because of the small SB (Fig. 15g). Large streamwise and crosswise Reynolds stresses exist near the main element of the clean airfoil at an AOA of 0° because of the early flow separation (Fig. 12). The Reynolds stresses gradually decrease with an increase in the AOA up to 12° by the delayed separation (Fig. 12), whereas it rapidly increases at an AOA of 16°. Large streamwise and crosswise Reynolds stresses are observed continuously on the upper surface of the flap element because of the persistence of the wake behind the main element.

Compared to the clean airfoil, small streamwise and crosswise Reynolds stresses are found on the upper surface of all the elements at all AOAs for the SLD case as shown in Fig. 17. However, the Reynolds stresses on the lower surface of the main and flap elements are large compared to those of the clean case at an AOA of 0° because of the effect of the stretched primary SB within the slat cove (see streamlines in Figs. 17a and b). As shown in Fig. 18, the magnitudes of the streamwise and crosswise Reynolds stresses for the non-SLD case are smaller than that of the clean case on the upper surface of all the elements at an AOA $\leq$ 4°, similar to our observation for the SLD case. However, the non-SLD case shows large streamwise and crosswise Reynolds stresses on the upper surface of the slat element, particularly at an AOA $\geq$ 8° because of the SBs created aft of the upwind horn-shaped ice as shown in Fig. 15. The peaks of the streamwise Reynolds stresses at an AOA $\geq$ 8° are obtained immediately following the attainment of the maximum thicknesses of the SBs aft of the upwind horn-shaped ice (blue crosses). Compared to these peaks, slightly weaker peaks of the crosswise Reynolds stresses are found further downstream. However, for the non-SLD case, enhanced turbulent activities exist on the upper surface of the main element at an AOA $\geq$ 8° (Figs. 18e–j). At an AOA of 12°, the peak of the streamwise Reynolds stress occurs at $x/c \approx 0.8$, similar to the position of the maximum thickness of the SB, whereas that of the crosswise Reynolds stress is located in the upstream position at $x/c \approx 0.7$. Compared to the streamwise

Reynolds stresses, the magnitude of the crosswise Reynolds stresses is relatively small near the upstream region of $x/c = 0.4$.

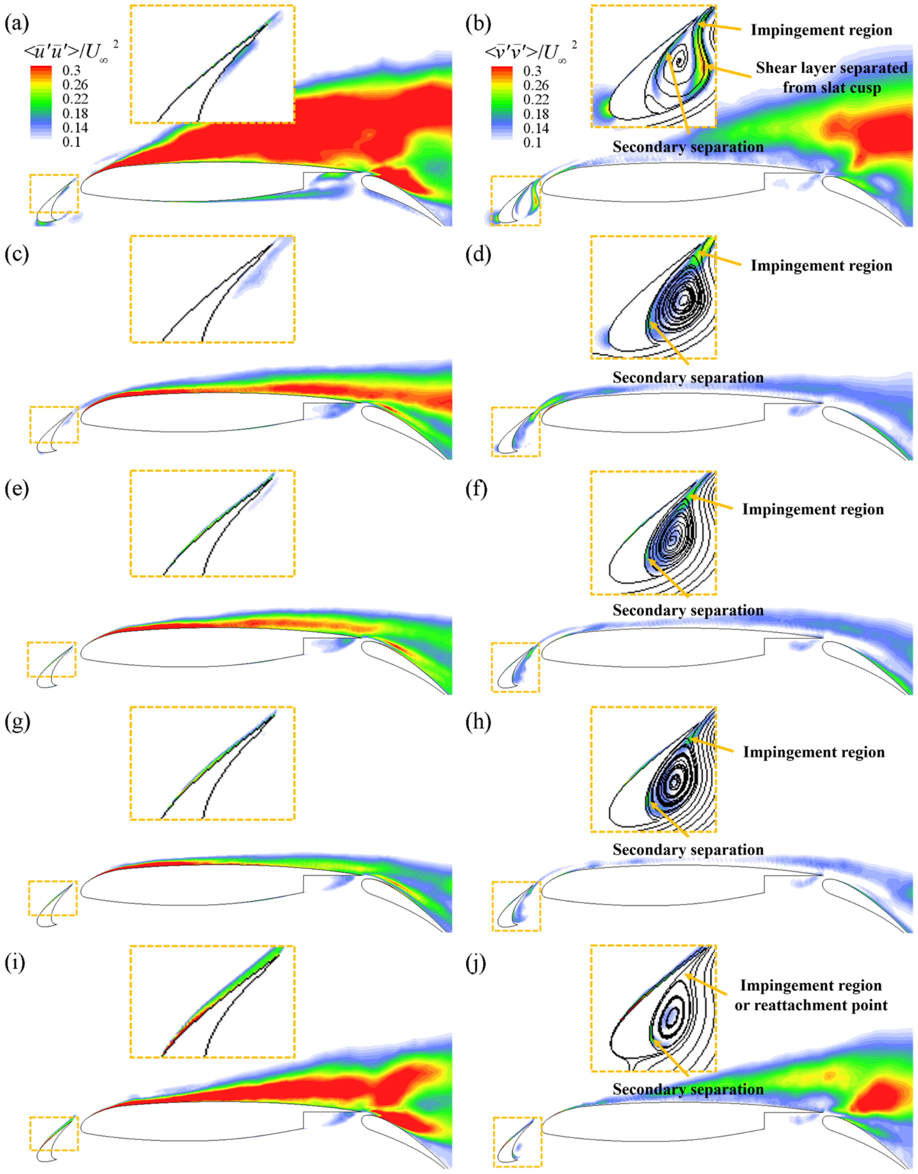

Fig. 16 Contours of streamwise (left) and crosswise (right) Reynolds stresses for clean airfoil: (a, b) AOA = 0º, (c, d) 4º, (e, f) 8º, (g, h) 12º, and (i, j) 16º.

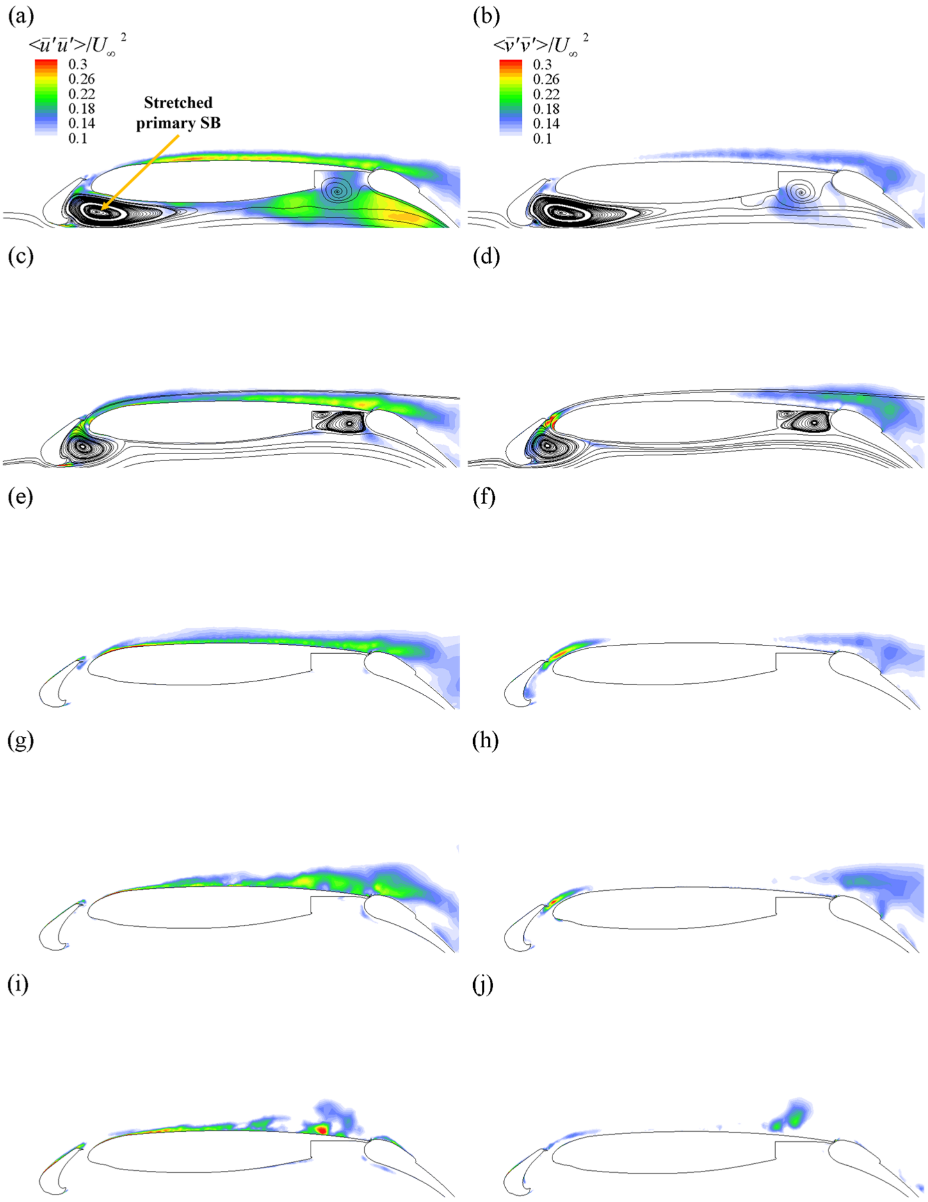

Fig. 17 Identical to those in Fig. 16, but for SLD case. The streamlines are superimposed at low AOAs.

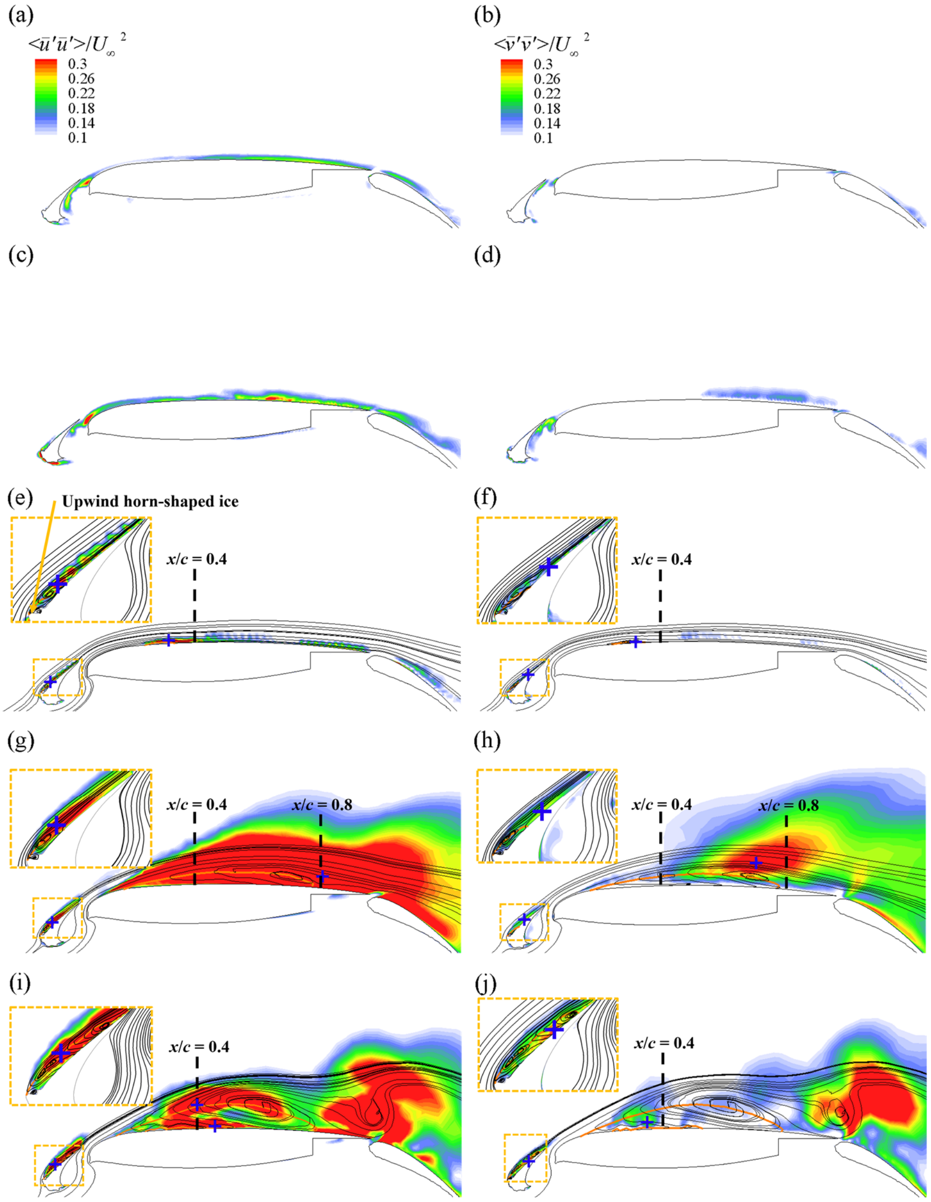

Fig. 18 Identical to those in Fig. 16, but for non-SLD case. Solid orange lines at high AOAs denote the mean stagnation lines on upper surfaces of slat and main elements. Blue crosses indicate peak locations of Reynolds stresses.

At an AOA of 16º, both the streamwise and crosswise Reynolds stresses on the upper surface of the main element decrease compared to those at an AOA of 12º, although strong Reynolds stresses are found above the flap gap. The decreased Reynolds stresses are closely related to the stabilization effects after a fast transition within the primary SB on the main element as the AOA increases from 12 to 16º [58,61].

3.2. Flow interaction

To examine how the aerodynamic characteristics (e.g., flow separation and Reynolds stresses) over the airfoils are created, the flow interactions around the multi-element airfoils are analyzed using the instantaneous velocity magnitude predicted by the LES method at a spanwise location (z/c = 0.02). The instantaneous velocity magnitude is calculated as $\overline{u}_{mag} = \sqrt{\overline{u}^2 + \overline{v}^2 + \overline{w}^2}$. Because the main element is a dominant contributor to determine the global aerodynamic performance (Fig. 7), we focus on flow interactions near the slat gap. An example of the flow interactions is shown in Fig. 19 using the instantaneous velocity magnitude at an AOA of 0º for the clean airfoil.

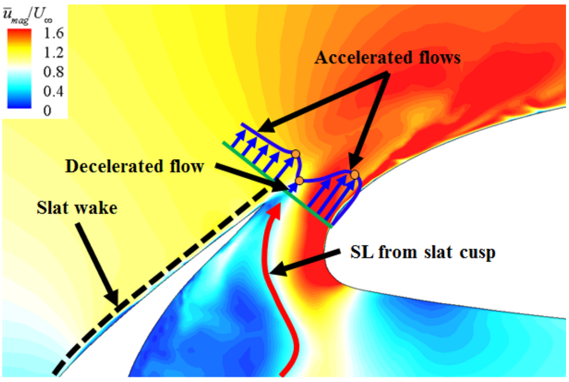

Fig. 19 Contour of instantaneous velocity magnitude at an AOA of 0º for clean case. Black dashed line represents the slat wake region, and blue solid line indicates an instantaneous velocity profile along the green solid line, respectively. Orange circles denote positions of large velocity inflections. Red solid line with arrow indicates SL trajectory shed from slat cusp.

A one-dimensional velocity profile near the slat trailing edge is superimposed along the green solid line (across the slat gap) to indicate the velocity inflections with various magnitudes. As shown, two accelerated flows are induced from the leading edge of the main element and the upper surface of the slat element. However, a slat wake created by a flow separation on the upper surface of the slat element (dashed lines) and a SL shed from the slat cusp (red arrow) generate a decelerated flow near the slat trailing edge. The velocity difference between the accelerated and decelerated flows results in a large velocity inflection point very close to the slat trailing edge (orange circle). Additional velocity inflection points are found within the two accelerated flows as highlighted by the orange circles. Because velocity inflections play an important role in triggering flow separation [62], it is worthwhile to examine how velocity inflections are modified by ice accretion with various AOAs.

Contours of the instantaneous velocity magnitudes for the clean, SLD, and non-SLD cases at AOAs of 0, 8, and 16° are shown in Figs. 20–22. The one-dimensional instantaneous velocity profiles at various distances from the surface are extracted at four reference positions (lines A–D, $0.05 \leq x/c \leq 0.13$) on the upper surface of the main element. As shown in Fig. 20(a) for the clean airfoil at an AOA of 0°, two acceleration flows exist near the leading edge of the main element and on the upper surface of the slat element. The presence of a significantly decelerated flow near the slat trailing edge leads to severe velocity inflections (orange circles along the black solid line in inset). When these velocity inflections with large velocity differences between the inflection points are transferred along the downstream direction (lines B–D), a flow separation is found to occur near the main leading edge (purple circles). The unsteady flow separation is closely associated with the evolution of vortices generated by large velocity inflections with an accompanying unsteady adverse pressure gradient (APG) effects (shown later). Because a large disturbance after the separation point accelerate the transition process, increased Reynolds stresses occur on the upper surface of the main element (Fig. 16a). Velocity inflections aft of the slat trailing edge (line A) are also found at an AOA of 8° as shown in Fig. 20(b). However, because the decelerated flow created by a SL shed from the slat cusp is weakened near the slat trailing edge with an increased distance L_B as shown in Fig. 15(d), the reduced velocity differences between the velocity inflection points decrease the effect of the velocity inflections. Thus, a delayed separation point (purple circles) is observed at an AOA of 8° with the decreased Reynolds stresses as shown in Figs. 16(e) and (f).

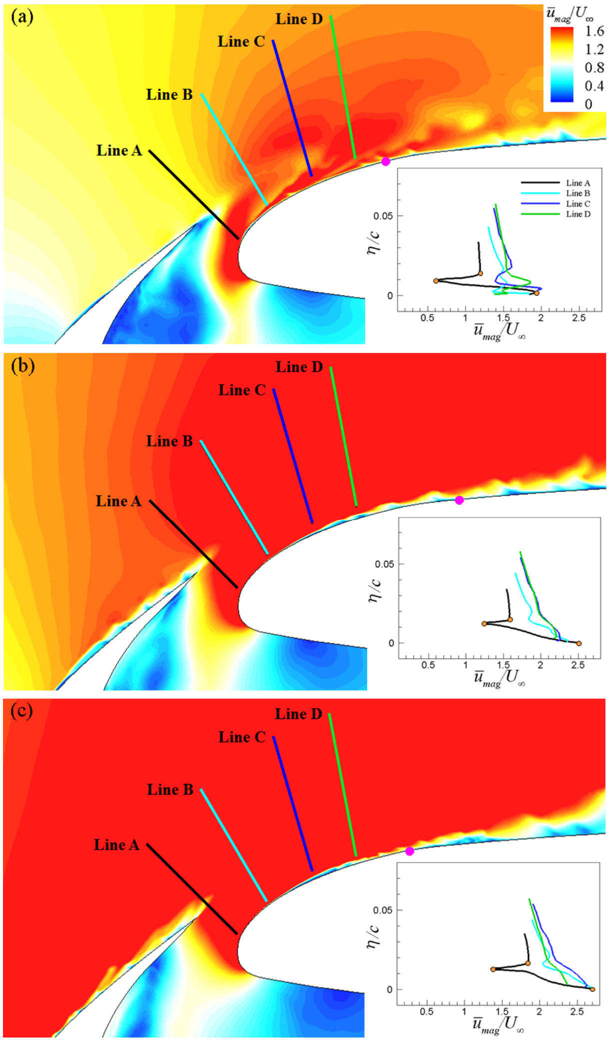

Fig. 20 Contours of instantaneous velocity magnitude for clean airfoil: (a) AOA = 0º, (b) 8º, and (c) 16º. Purple circles indicate separation points on the main element. One-dimensional velocity profiles along lines A–D are plotted in insets. Orange circles in insets denote positions of large velocity inflections along line A.

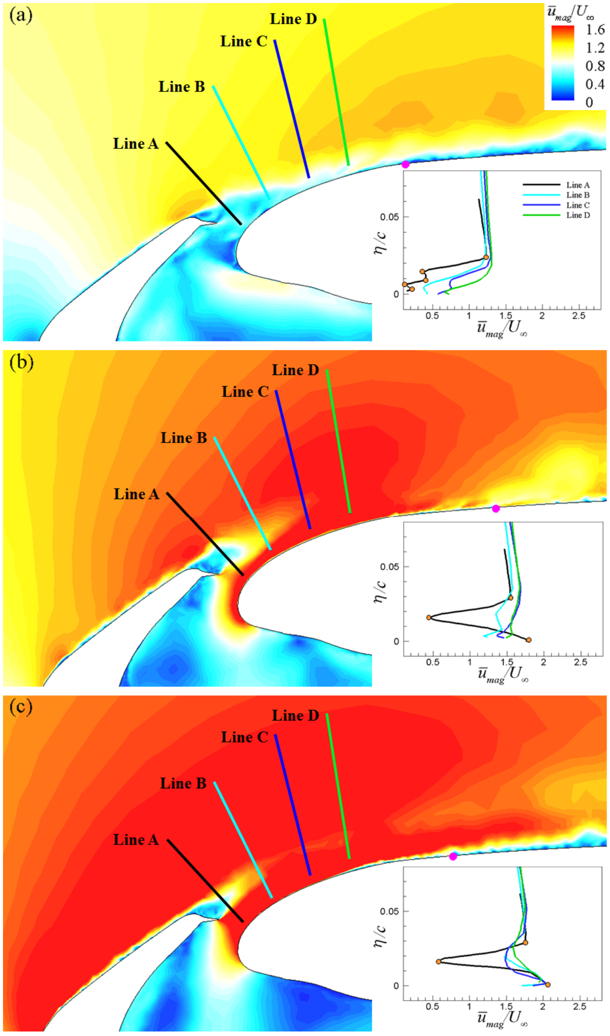

Fig. 21 Identical to those in Fig. 20, but for SLD case.

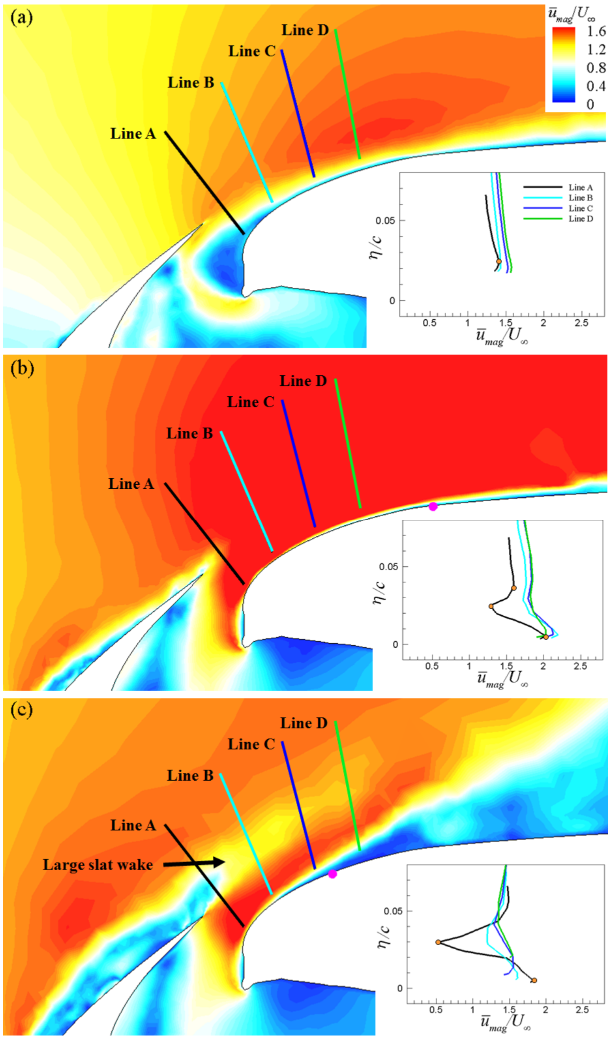

Fig. 22 Identical to those in Fig. 20, but for non-SLD case.

In contrast, as the AOA increases further, highly accelerated flows on the upper surfaces of the slat and main elements at an AOA of 16º (Fig. 12) result in a strong velocity inflection impact (see inset of Fig. 20c). This leads to a separation point further upstream than that at an AOA of 8º (purple circles). The early flow separation with increased velocity differences enhances the Reynolds stresses aft of the separation point on the upper surface of the main element (Figs. 16i and j). However, the strength of the Reynolds stresses is not as strong as that at an AOA of 0º because of the slightly delayed separation.

Compared to the clean airfoil, the SLD case at an AOA of 0º in Fig. 21(a) shows a delayed flow separation because the secondary SBs created near the main leading edge and the slat trailing edge (Fig. 15) generate a decelerated flow near the main leading edge, resulting in weaker velocity inflections. As shown in Fig. 21(b), as the AOA increases to 8º, velocity inflections with large velocity differences are found near the slat trailing edge (black line) because of the combined effects of the accelerated and decelerated flows. However, the impact of the velocity inflections decreases significantly along the downstream direction (lines B–D) with small velocity differences between the velocity inflection points. The delayed flow separation at an AOA of 8º compared to that at an AOA of 0º (purple circles) indicates that the velocity inflections in the downstream region are important in determining the flow separation. As shown in Fig. 21(c), as the AOA increases to 16º, velocity inflections with large velocity differences are found near the slat trailing edge (line A), consistent with the observation at an AOA of 8º. In addition to the large velocity differences along line A, the enhanced velocity inflections with relatively large velocity differences along the downstream direction compared to those at an AOA of 8º suggest the presence of an early flow separation.

As shown in Fig. 22(a), for the non-SLD case at an AOA of 0º, a velocity inflection with a very small velocity difference exists along line A because the absence of the secondary SB near the slat trailing edge does not introduce a decelerated flow aft of the slat trailing edge (compare Figs. 21a and 22a). As a result, a significantly delayed flow separation is observed with small Reynolds stresses (Figs. 14a and 18a) on the upper surface of the main element compared to that of the clean and SLD cases (Figs. 20a and 21a). Because the flow separation is significantly delayed for the non-SLD case at an AOA of 0º, the separation point is beyond the field of view shown in Fig. 22(a). As the AOA increases (Figs. 22b and c), the generation of secondary SBs aft of the upwind horn-shaped ice on the slat element (Figs. 15c, f, and i) results in a large slat wake near the slat trailing edge, leading to a large decelerated region behind the slat trailing edge. Although the velocity differences between the adjacent inflection points shown in Fig. 22(c) are relatively small compared to those of the cases shown in Figs. 20 and 21, the decelerated flow through a wide range of the wall-normal extent along line A penetrates into the downstream direction while maintaining its profile shape. Thus, the increased impact of the velocity inflections in the downstream direction accelerates the flow separation on the main element at an AOA ≥ 8º compared to that of the clean and SLD cases.

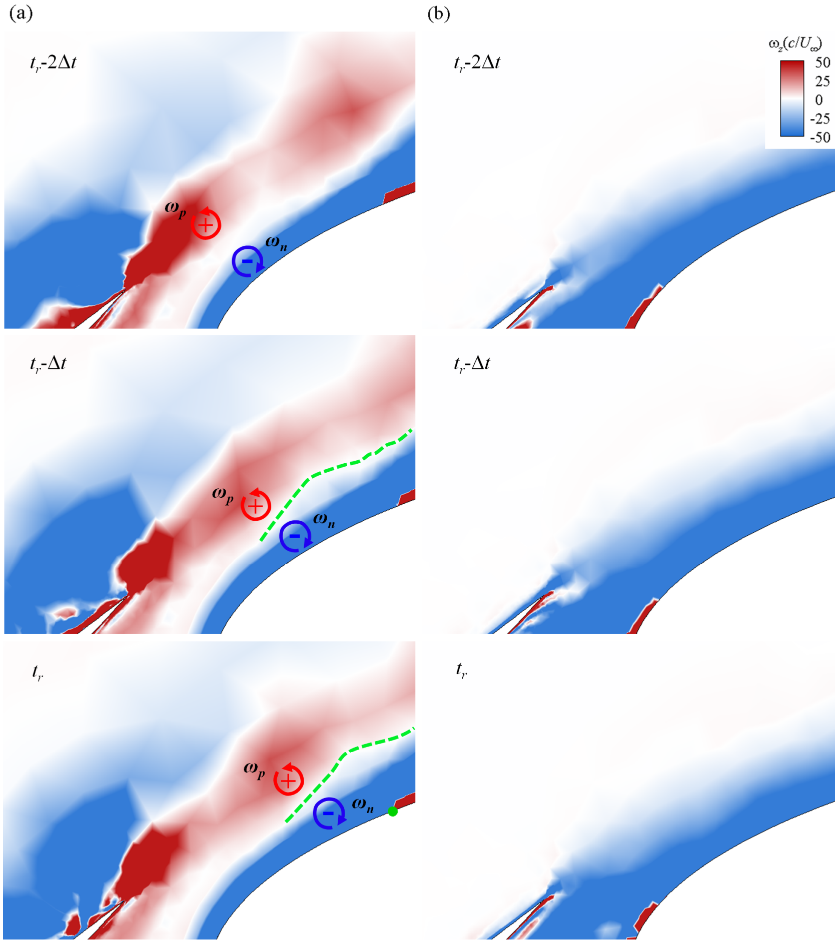

Fig. 23 Time-evolving instantaneous spanwise vorticity $\omega_z(c/U_\infty)$ for non-SLD case: (a) AOA = 16º and (b) AOA = 0º. The time interval is Δt=0.03876c/U_∞. Red and blue circles with arrows denote the rotational directions of positive (ω_p) and negative (ω_n) spanwise vorticities, respectively. Green dashed lines indicate interfaces between positive and negative spanwise vorticities. Green circle at $t = t_r$ in (a) represents a vortex-induced separation point on the main element.

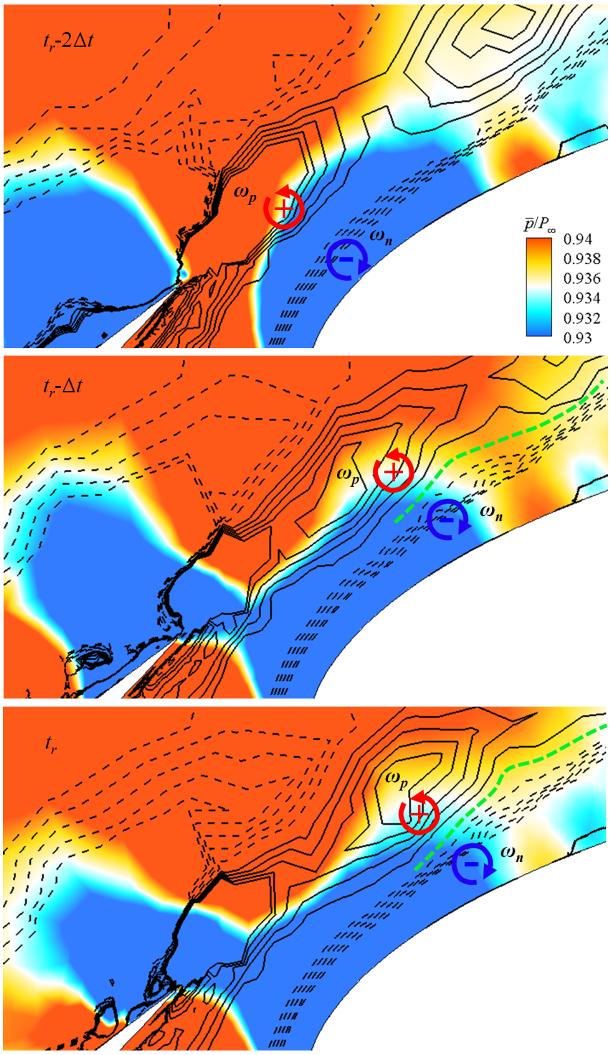

Fig. 24 Contours of instantaneous pressure field ($\overline{p} / P_\infty$) at an AOA of 16° for non-SLD case. P_∞ indicates reference pressure of 10^5 Pa. Contours at $t = t_r$, t_r-Δt and t_r-2Δt are extracted at the same instant in Fig. 23. Line contours represent instantaneous spanwise vorticity $\omega_z(c/U_\infty)$, and contour level is varied from -30 to 30 with an interval of 6 (A zero-line is omitted). Solid and dashed lines indicate the positive and negative contour values respectively. Red and blue circles with arrows denote the rotational directions of positive (ω_p) and negative (ω_n) spanwise vorticities, respectively. Green dashed lines indicate interfaces between positive and negative spanwise vorticities.

The spatial and temporal evolution of the vorticity field provides a clear picture of the unsteady separation process, because flow separation can be triggered with concentrated vortices moving close to a wall [63-64]. Fig. 23(a) shows time-evolving contours of the instantaneous spanwise vorticity at an AOA of 16º for the non-SLD case. The plot at $t = t_r$ in Fig. 23(a) is extracted at the same instant in Fig. 22(c) to investigate relationship between flow separation and velocity inflections. At $t = t_r-2\Delta t$, a positive vorticity ω_p is shown to be generated by the velocity inflections with the large velocity differences (Fig. 22c). As the positive vortex moves downstream, it interacts with a negative vorticity ω_n created by the vortex shedding from the main leading edge. Because the rotational direction of ω_p is counter-clockwise, a vortex-induced velocity by ω_p leads to an upward deflection of an interface between the two vorticities at $t = t_r-\Delta t$ (green dashed lines). With time further, the interface with an inclination angle to the wall is observed in a wide range of the downstream region. The continuous deflection of ω_n into the outer region introduces a new positive vorticity with an opposite sign to ω_n very close to the wall at $t = t_r$, thereby an early flow separation (Fig. 22c). In contrast to the observation at an AOA of 16º, the time-evolving plot of the instantaneous spanwise vorticity at an AOA of 0º for the non-SLD case in Fig. 23(b) shows the absence of a strong positive vorticity at $t = t_r-2\Delta t$ due to little velocity inflection (Fig. 22a). Compared to the vortex-induced separation at an AOA of 16º, a positive pressure gradient in a downstream region of a maximum thickness of an airfoil plays an important role to generate a flow separation at the low AOA [65].

The vortex-induced unsteady separation found in this study is similar to previous findings by Harvey and Perry [63], Didden and Ho [64] and Cassel and Conlisk [66]. Harvey and Perry [63] placed a half span rectangular wing in a wind tunnel to generate a single trailing-vortex, and examined the evolution of this vortex as it passed over a moving floor in a downstream region. They found that the cross flow induced by this vortex results in APG effect to a boundary layer developed by the moving floor. When the vortex approached the floor, the effect of this APG was sufficiently strong to generate a flow separation. Didden and Ho [64] conducted an experimental study of an unsteady separation when ring vortices impinged onto a flat plate. The results showed that an accelerated flow induced by the primary ring vortices causes APG effect. The retarded flow by the APG formed a strong shear layer, and a secondary vortex induced by instability of this shear layer was directly associated to the onset of unsteady separation. According to the previous studies, contours of the instantaneous pressure fields are investigated with time to identify generation of an APG by the spanwise vortices in Fig. 24. At an AOA of 16º for the non-SLD case, strong and weak pressure fields are observed in the decelerated and accelerated regions (Fig. 22) at $t = t_r\text{-}2\Delta t$. As a flow acceleration is induced by the cooperative work of ω_p and ω_n (i.e., vortex-induced velocity) along the interface, a strong APG is found to occur near the interface at $t = t_r\text{-}\Delta t$ and $t = t_r$, creating a vortex-induced separation.

3.3. Energy spectrum of pressure fluctuations

Significant research has been conducted to improve our understanding of the unsteady SB characteristics of single- and multi-element airfoils [11,30,67-70]. Previous studies have focused on the SBs within the slat coves of multi-element clean airfoils [30,68-70] or SBs aft of the horn-shaped ice of a single-element iced airfoil [11,67]. In this section, we explore the unsteady characteristics of the SBs of a multi-element iced airfoil by the spectral analysis of pressure fluctuations [11,67,71]. Here, only the non-SLD case is considered because it has unique unsteady flow patterns (Fig. 14) compared to those of the clean and SLD cases.

Fig. 25 shows the eight probe points P1–P8 located near the upwind horn-shaped ice of the slat element ($-0.1 \leq x/c \leq -0.07$) and on the upper surface of the main element ($0.3 \leq x/c \leq 0.36$) with respect to the AOA used to obtain the time-series pressure data. In the inset, contours of $Q(c/U_\infty)^2$ [72] show the shedding vortices aft of the upwind horn-shaped ice of the slat element. After the flow fields statistically reach steady states based on a surface pressure coefficient, the pressure data are collected at an interval of 10^{-6} s. The sampling time duration is approximately 0.05 s, which is sufficient to capture peak frequencies associated with the crucial unsteady flow characteristics (e.g., vortex shedding) [67]. The pressure fluctuations are calculated using $\overline{p}' = \overline{p} - \langle \overline{p} \rangle$, and a Hamming window [73] is applied to each pressure fluctuation signal to suppress the spectral leakage and Gibb's phenomenon. Because the recording time is sufficiently long, this window function results in a negligible distortion of the power spectral density (PSD). The pressure fluctuation signal of the given time domain is evaluated in the frequency domain using the fast Fourier transform (FFT) method.

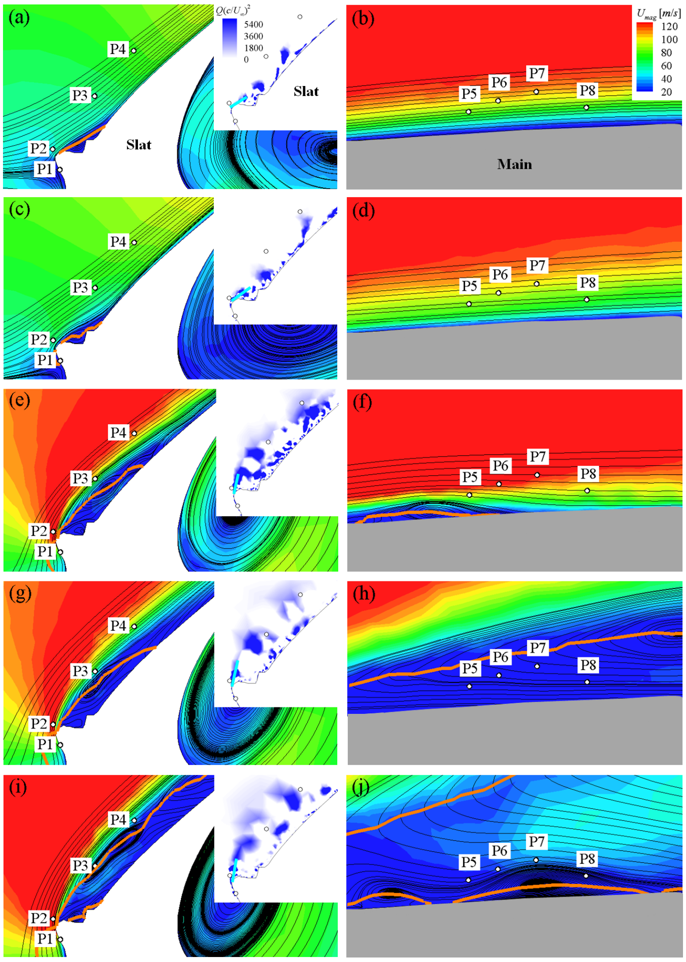

Fig. 25 Contours of the mean velocity magnitude with streamlines for non-SLD case: (a, b) AOA = 0º, (c, d) 4º, (e, f) 8º, (g, h) 12º, and (i, j) 16º. White circles indicate probe positions. In each figure, orange solid lines denote mean stagnation lines on upper surfaces of slat and main elements. Instantaneous contours of $Q(c/U_\infty)^2$ are depicted in insets, and solid sky-blue lines indicate a linear fit of three vortex core locations aft of upwind horn-shaped ice on the slat element.

Fig. 26 shows the PSD of the pressure fluctuations at probe locations P1–P4 for the non-SLD case at AOAs of 0, 4, 8, 12, and 16°. The PSD of the pressure fluctuations is characterized by various strong peaks. In particular, the PSD at P1 and P2 has many strong peaks with an interval of $\Delta fc/U_\infty = 14$ at all AOAs (see orange vertical lines), although one strong peak at $fc/U_\infty = 34$ occurs at an AOA of 0° (purple vertical line). The dominant low-frequency peak ($fc/U_\infty = 14$) is related to the initiation of the vortex shedding aft of the upwind horn-shaped ice (see inset in Fig. 25). The frequencies in the AOA range 0–12° at P1 and P2 correspond to non-dimensional Strouhal numbers, St_b, in the range 0.26–0.7 based on the SB length (L_T in Table 4) and the freestream velocity U_∞. These St_b values are comparable to those of a regular vortex shedding mode (0.5–0.75) for a single-element iced airfoil with ice horns at an AOA of 0 to 8° [11,67,71]. At an AOA of 16°, the value of St_b (= 1.62) is significantly greater because of the increased bubble length L_T in the presence of SBs along the upper surface of the slat element (green crosses in Fig. 15i). The high-frequency peaks ($fc/U_\infty = 28$, 42, 56, and 70) at P1 and P2 are attributed to the oscillations of the harmonic shedding vortices aft of the upwind horn-shaped ice. The magnitude of the peaks gradually decreases in the further downstream region from P1 to P4 because the resolved kinetic energy is transferred into the inertial subrange owing to the viscous dissipation [74]. The higher dominant frequency peak at an AOA of 0° is the result of the relatively small shedding vortex (see inset of Fig. 25). The disappearance of the high-frequency peaks at P3 and P4 is induced by the merging of the small shedding vortices as they move downstream. As the AOA increases, the magnitude of the peaks is gradually enhanced up to an AOA of 12° at P1–P4 because the shedding vortices at low AOAs reach the wall faster (see sky-blue solid lines in inset of Fig. 25). However, the peaks at an AOA of 16° are slightly smaller than those at an AOA of 12° at P3 and P4 because of the influence of the reference positions within the SB (Fig. 25i).

Fig. 27 shows the PSD of the pressure fluctuations at probe points P5–P8 near the secondary SB over the main element. At an AOA of 16°, a weak peak occurs at $fc/U_\infty \approx 2.5$ (orange vertical lines) corresponding to $St_b \approx 0.62$, where St_b is defined based on the freestream velocity U_∞ and the secondary SB length ($b_2/c \approx 0.25$ in Fig. 14i). The unsteadiness by the secondary SBs (Fig. 25j) is characterized by a streamwise oscillation of the flow reattachment [71]. This peak ($fc/U_\infty \approx 2.5$) is similar to the Strouhal number of the regular vortex mode used in previous experimental and numerical studies [67,71], even though the SB in the previous results was found aft of a horn-ice shape for a single-element iced airfoil. In addition, the present Strouhal number peak of approximately 0.62 is in good agreement with the observations of previous studies on various separated flows [75-77]. In a backward-facing step flow, Eaton and Johnston [75] reported a Strouhal number of 0.52 near the reattachment through the power spectrum of the streamwise velocity fluctuations. Kiya and Sasaki [76] found values of 0.6–0.65 for a shedding vortex on a blunt flat plate. Cherry et al. [77] reported a shedding frequency of 0.7 using the SL velocity fluctuations on a flat plate. As the AOA decreases, the magnitude of the PSD decreases at a low frequency ($fc/U_\infty < 2$) because of the absence of turbulent activities at a low AOA. The low PSD at an AOA of 16º compared to that at an AOA of 12º is attributed to the weakened turbulence on the main element (Figs. 18g–j).

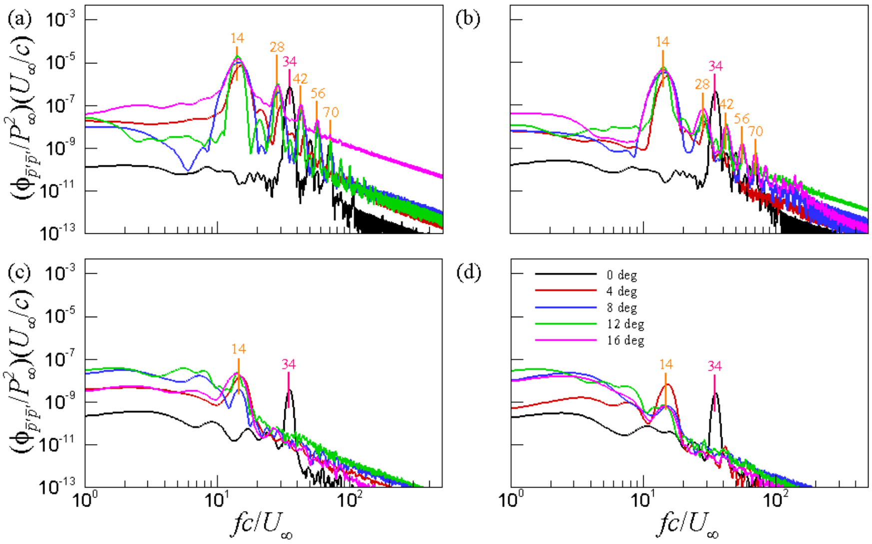

Fig. 26 PSD of pressure fluctuations for non-SLD case at probe point: (a) P1, (b) P2, (c) P3, and (d) P4. P_∞ indicates reference pressure of 10^5 Pa.

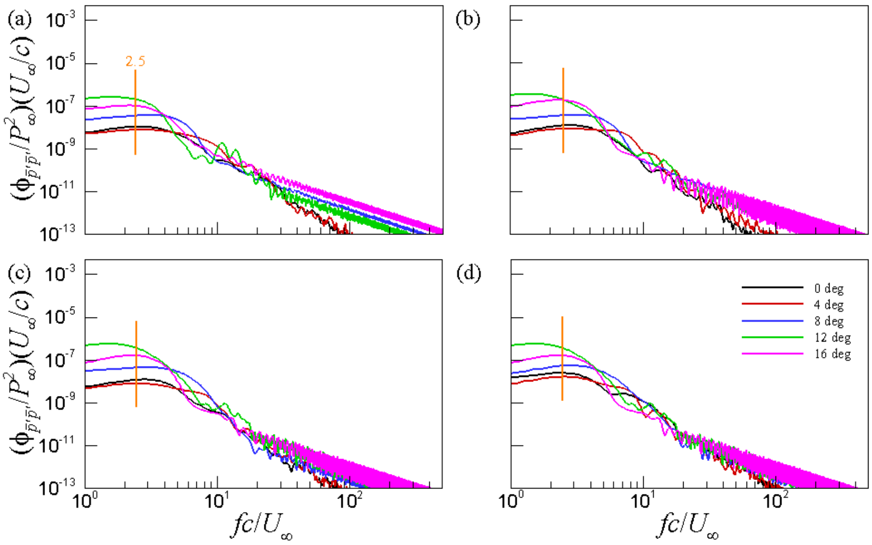

Fig. 27 Identical to those in Fig. 26, but for non-SLD case at probe point: (a) P5, (b) P6, (c) P7, and (d) P8.

4. Summary and conclusion

In the present study, we performed LESs around three element iced airfoils under SLD and non-SLD conditions to examine the unique flow characteristics. Direct comparison of our LES data and independently simulated URANS data with previous experimental data showed that the LES provides a good prediction of the aerodynamics of the clean and iced airfoils. However, the URANS data overestimated the suction peaks on the slat and main elements at an AOA ≥ 4º for the clean and iced airfoils because the downstream stagnation points led to accelerated flows on the suction side on the slat and main elements. The difference in the suction peaks between the URANS and LES data increased with an increase in the AOA because of the inaccurate URANS prediction of the primary and secondary SBs within the slat coves. Furthermore, the flow separations predicted by the URANS simulation were delayed on the main element regardless of the AOA, resulting in inaccurate lift and drag coefficients. The delayed flow separation from the URANS simulation failed to identify the primary and secondary SBs related to the pressure recovery process on the upper surface of the main element at high AOAs for the non-SLD case. On the flap element, the flow separations predicted by the URANS method were delayed at all AOAs for both the clean and iced airfoils, except for AOAs of 4 and 8º for the clean airfoil.

The introduction of ice accretion on the surface of the airfoil resulted in a total lift loss, in particular on the main element with an accompanying reduction of the suction peaks, consistent with previous studies. In addition to a primary SB created by a SL shed from the slat leading edge (or cusp), the ice accretion near the slat leading and trailing edges and the main leading edge induced many secondary SBs under the SLD and non-SLD conditions compared to that of the clean airfoil. The interaction between the primary and secondary SBs within a slat cove led to the streamwise stretching of the primary SB, and the modified trajectory of the primary SB reduced the mass flow rate through the gap, thereby the lift loss with the decreased suction peaks. As the AOA increased, the strength of the secondary SB near the leading edge of the main element decreased for the SLD and non-SLD cases, and thus the mass flow rate increased. Compared to the non-SLD case, the stretching of the primary SB was significant for the SLD case, resulting in a significant reduction in the mass flow rate and lift loss. The reattachment length associated with the mean stagnation lines on the upper surface of the slat element for the non-SLD case was estimated using the quadratic equation proportional to the square value of the AOA.

Based on the contours of the instantaneous velocity magnitude for the clean and iced airfoils, the combination of accelerated and decelerated flows near a slat gap allowed the velocity inflections with large velocity differences to have a strong impact on the flow characteristics over the main element. The accelerated flows were induced from the main leading edge and upper surface of the slat element, and the decelerated flow was generated by a flow separation on the upper surface of the slat element (slat wake) and a SL shed from the slat cusp. As the AOA for the clean airfoil increased up to 12º, the weakened decelerated flow by a SL shed from the slat cusp near the slat trailing edge reduced the velocity differences between the velocity inflection points, and as a result, the delayed separation point was found with the decreased Reynolds stresses on the main element. However, as the AOA increased to 16º, the velocity inflections significantly impacted the flow transition by accelerating the flows on both the upper surfaces of the slat and main elements, leading to an early flow separation.

For the SLD and non-SLD cases, the velocity inflections had a weak impact aft of the slat trailing edge to delay the flow separations because of the presence of the secondary SBs near the slat gap. However, the secondary SBs aft of the upwind horn-shaped ice of the slat element for the non-SLD case generated a large slat wake near the slat trailing edge with an AOA ≥ 8º. The decelerated flow by the slat wake through a wide range of the wall-normal extent behind the slat trailing edge contributed to the strong impact of the velocity inflections along the downstream direction, and thus early flow separations occurred along with increased Reynolds stresses on the main element. Detailed analysis using the time-evolving instantaneous spanwise vorticity and pressure fields showed that a strong positive vorticity generated by the large velocity inflections near the slat trailing edge plays a significant role to occur an early vortex-induced separation by the APG effect.

The spectral analysis of the pressure fluctuations near the upwind horn-shaped ice on the slat element (P1 and P2) for the non-SLD case revealed a low-frequency peak ($fc/U_\infty = 14$) at all AOAs except for 0º because of the vortex shedding aft of the upwind horn-shaped ice. However, the relatively small shedding vortex at an AOA of 0º led to a higher frequency peak ($fc/U_\infty = 34$). In addition, several high-frequency peaks ($St_b = 0.26$–1.62) at an interval of $\Delta fc/U_\infty = 14$ were found immediately aft of the upwind horn-shaped ice at all AOAs except for 0º because of the oscillations of the harmonic shedding vortices. However, the high-frequency peaks disappeared further downstream (P3 and P4) as the small shedding vortices merged. The PSD near the secondary SBs on the upper surface of the main element (P5–P8) suggested that the unsteadiness by the secondary SBs at high AOAs is represented by a dominant low-frequency peak, $fc/U_\infty \approx 2.5$ ($St_b \approx 0.62$) due to a streamwise oscillation of flow reattachment. An understanding of the complicated flow patterns of the SLD and non-SLD cases in this study will provide valuable insights for the improvement of the prediction performance of ice accretion simulations for multi-element airfoils. It will also provide a basis for the design of practical ice protection systems for aircraft.

Acknowledgements

This work was supported by the National Research Foundation of Korea (NRF) Grant funded by the Ministry of Science, ICT and Future Planning (NRF-2017R1A5A1015311).

References

[1] M.B. Bragg, A.P. Broeren, L.A. Blumenthal, Iced-airfoil aerodynamics, Prog. Aerosp. Sci. 41 (2005) 323-418.

[2] T. Liu, K. Qu, J. Cai, S. Pan, A three-dimensional aircraft ice accretion model based on the numerical solution of the unsteady Stefan problem, Aerosp. Sci. Technol. 93 (2019) 105328.

[3] L.P. Raj, K. Yee, R.S. Myong, Sensitivity of ice accretion and aerodynamic performance degradation to critical physical and modeling parameters affecting airfoil icing, Aerosp. Sci. Technol. 98 (2020) 105659.

[4] H. Fatahian, H. Salarian, M.E. Nimvari, J. Khaleghinia, Effect of Gurney flap on flow separation and aerodynamic performance of an airfoil under rain and icing conditions, Acta Mech. Sin. (2020) 1-19.

[5] G.B. Ahn, K.Y. Jung, R.S. Myong, H.B. Shin, W.G. Habashi, Numerical and experimental investigation of ice accretion on rotorcraft engine air intake, J. Aircr. 52 (2015) 903-909.

[6] V. Abdollahi, W.G. Habashi, M. Fossati, Multi-phase smoothed particle hydrodynamics modeling of supercooled large droplet dynamics for in-flight icing conditions, Aerosp. Sci. Technol. 82 (2018) 252-261.

[7] Y. Cao, W. Tan, Z. Wu, Aircraft icing: An ongoing threat to aviation safety, Aerosp. Sci. Technol. 75 (2018) 353-385.

[8] M.B. Bragg, W.J. Coirier, Detailed measurements of the flow field in the vicinity of and airfoil with simulated glaze ice, in: 23rd AIAA Aerospace Sciences Meeting, American Institute of Aeronautics and Astronautics, 1985.

[9] C.M. Brown, R.F. Kunz, M.P. Kinzel, J. Lindau, Large eddy simulation of airfoil ice accretion aerodynamics, in: 6th AIAA Atmospheric and Space Environments Conference, American Institute of Aeronautics and Astronautics, 2014.

[10] Y. Zhang, W.G. Habashi, R.A. Khurram, Zonal detached-eddy simulation of turbulent unsteady flow over iced airfoils, J. Aircr. 53 (2016) 168-181.

[11] M. Xiao, Y. Zhang, F. Zhou, Numerical study of iced airfoils with horn features using large-eddy simulation, J. Aircr. 56 (2018) 94-107.

[12] D. Reckzeh, Aerodynamic design of the high-lift-wing for a Megaliner aircraft, Aerosp. Sci. Technol. 7 (2003) 107-119.

[13] J. Shin, P. Wilcox, V. Chin, D. Sheldon, Icing test results on an advanced two-dimensional high-lift multi-element airfoil, in: 12th Applied Aerodynamics Conference, American Institute of Aeronautics and Astronautics, 1994.

[14] D. Miller, J. Shin, D. Sheldon, A. Khodadoust, P. Wilcox, T. Langhals, Further investigations of icing effects on an advanced high-lift multi-element airfoil, in: 13th AIAA Applied Aerodynamics Conference, American Institute of Aeronautics and Astronautics, 1995.

[15] C. Zhang, F. Wang, W. Kong, H. Liu, The characteristics of SLD icing accretions and aerodynamic effects on high-lift configurations, in: 33rd AIAA Applied Aerodynamics Conference, American Institute of Aeronautics and Astronautics, 2015.

[16] R. Ashenden, J.D. Marwitz, Turboprop aircraft performance response to various environmental conditions, J. Aircr. 34 (1997) 278-287.

[17] S. Lee, M.B. Bragg, Experimental investigation of simulated large-droplet ice shapes on airfoil aerodynamics, J. Aircr. 36 (1999) 844-850.

[18] L.P. Raj, J.W. Lee, R.S. Myong, Ice accretion and aerodynamic effects on a multi-element airfoil under SLD icing conditions, Aerosp. Sci. Technol. 85 (2019) 320-333.

[19] J. Pan, E. Loth, Detached eddy simulations for airfoil with ice shapes, in: 42nd AIAA Aerospace Sciences Meeting and Exhibit, American Institute of Aeronautics and Astronautics, 2004.

[20] Y. Cao, K. Chen, J. Sheridan, Flowfield simulation and aerodynamic performance analysis of complex iced aerofoils with hybrid multi-block grid, Proc. Inst. Mech. Eng. G: J. Aerosp. Eng. 222 (2008) 417-422.

[21] J.H. Jo, L.P. Raj, Y.M. Lee, J.H. Lee, R.S. Myong, Computational simulation of flows over a ridge iced airfoil using RANS and LES, J. Comput. Fluids Eng. 24 (2019) 8-18.

[22] P. Mogili, D. Thompson, Y. Choo, H. Addy, RANS and DES computations for a wing with ice accretion, in: 43rd AIAA Aerospace Sciences Meeting and Exhibit, American Institute of Aeronautics and Astronautics, 2005.

[23] A. Lorenzo, E. Valero, V. Depablo, DES/DDES post-stall study with iced airfoil, in: 49th AIAA Aerospace Sciences Meeting including the New Horizons Forum and Aerospace Exposition, American Institute of Aeronautics and Astronautics, 2011.

[24] M. Costes, F. Moens, Advanced numerical prediction of iced airfoil aerodynamics, Aerosp. Sci. Technol. 91 (2019) 186-207.

[25] M. Duclercq, V. Brunet, F. Moens, Physical analysis of the separated flow around an iced airfoil based on ZDES simulations, in: 4th AIAA Atmospheric and Space Environments Conference, American Institute of Aeronautics and Astronautics, 2012.

[26] S. Deck, N. Renard, Towards an enhanced protection of attached boundary layers in hybrid RANS/LES methods, J. Comput. Phys. 400 (2020) 108970.

[27] P.R. Spalart, S. Deck, M.L. Shur, K.D. Squires, M.K. Strelets, A. Travin, A new version of detached-eddy simulation, resistant to ambiguous grid densities, Theor. Comp. Fluid Dyn. 20 (2006) 181-195.

[28] S. Deck, Recent improvements in the zonal detached eddy simulation (ZDES) formulation, Theor. Comp. Fluid Dyn. 26, (2012) 523-550.

[29] W. Lu, P. Liu, H. Guo, T. Hu, Investigation on tones due to self-excited oscillation within leading-edge slat cove at different angles of attack: Frequency and intensity, Aerosp. Sci. Technol. 91 (2019) 59-69.

[30] H.K. Jawahar, R. Theunissen, M. Azarpeyvand, C.R.I. Silva, Flow characteristics of slat cove fillers, Aerosp. Sci. Technol. 100 (2020) 105789.

[31] A. Khodadoust, C. Dominik, J. Shin, D. Miller, Effect of in-flight ice accretion on the performance of a multielement airfoil, AHS/SAE International Icing Symposium (1995).

[32] J. Shao, C. Zhang, Numerical analysis of the flow around a circular cylinder using RANS and LES, Int. J. Comput. Fluid Dyn. 20 (2006) 301-307.

[33] M. Zhao, Y. Zhao, Z. Liu, Dynamic mode decomposition analysis of flow characteristics of an airfoil with leading edge protuberances, Aerosp. Sci. Technol. 98 (2020) 105684.

[34] P.L. Roe, Characteristic-based schemes for the Euler equations, Annu. Rev. Fluid Mech. 18 (1986) 337-365.

[35] F. Mishriky, P. Walsh, Towards understanding the influence of gradient reconstruction methods on unstructured flow simulations, Trans. Can. Soc. Mech. Eng. 41 (2017) 169-179.

[36] P. Moin, K. Squires, W. Cabot, S. Lee, A dynamic subgrid-scale model for compressible turbulence and scalar transport, Phys. Fluids 3 (1991) 2746-2757.

[37] J. Smagorinsky, General circulation experiments with the primitive equations: I. The basic experiment, Mon. Weather Rev. 91 (1963) 99-164.

[38] M. Germano, U. Piomelli, P. Moin, W.H. Cabot, A dynamic subgrid-scale eddy viscosity model, Phys. Fluids 3 (1991) 1760-1765.

[39] L. Casadei, L. Könözsy, N.J. Lawson, Unsteady detached-eddy simulation (DES) of the Jetstream 31 aircraft in one engine inoperative (OEI) condition with propeller modelling, Aerosp. Sci. Technol. 91 (2019) 287-300.

[40] P. Beaudan, P. Moin, Numerical experiments on the flow past a circular cylinder at sub-critical Reynolds number, Report No. TF-62, Stanford University (1994) 1-44.

[41] R. Mittal, P. Moin, Suitability of upwind-biased finite difference schemes for large-eddy simulation of turbulent flows, AIAA J. 35 (1997) 1415-1417.

[42] W. Cheng, D.I. Pullin, R. Samtaney, W. Zhang, W. Gao, Large–eddy simulation of flow over a cylinder with Re_D from 3.9×10^3 to 8.5×10^5: A skin-friction perspective, J. Fluid Mech. 820 (2017) 121-158.

[43] L.N. Jenkins, D.H. Neuhart, C.B. McGinley, M.M. Choudhari, M.R. Khorrami, Measurements of unsteady wake interference between tandem cylinders, in: 36th AIAA Fluid Dynamics Conference and Exhibit, American Institute of Aeronautics and Astronautics, 2006.

[44] M. Papadakis, K.E. Hung, G.T. Vu, H.W. Yeong, C.S. Bidwell, M.D. Breer, T.J. Bencic, Experimental investigation of water droplet impingement on airfoils, finite wings, and an S-duct engine inlet, NASA Glenn Research Center, 2002.

[45] W.O. Valarezo, C.J. Dominik, R.J. Mcghee, Reynolds and Mach number effects on multielement airfoils, NASA Langley Research Center, 1992.

[46] I. Mary, P. Sagaut, Large eddy simulation of flow around an airfoil near stall, AIAA J. 40 (2002) 1139-1145.

[47] M.M. Choudhari, M.R. Khorrami, Effect of three-dimensional shear-layer structures on slat cove unsteadiness, AIAA J. 45 (2007) 2174-2186.

[48] M. Galbraith, M. Visbal, Implicit large eddy simulation of low Reynolds number flow past the SD7003 airfoil, in: 46th AIAA Aerospace Sciences Meeting and Exhibit, American Institute of Aeronautics and Astronautics, 2008.

[49] C. Gleyzes, Opération décrochage. Résultats des essais à la soufflerie F2, ONERA Internal Report, 1988.

[50] D. You, W. Bromby, Large-eddy simulation of unsteady separation over a pitching airfoil at high Reynolds number, in: Proceedings of the Seventh International Conference on Computational Fluid Dynamics (ICCFD7) (2012) 9-13.

[51] P.F. Lorber, F.O. Carta, Airfoil dynamic stall at constant pitch rate and high Reynolds number, J. Aircr. 25 (1988) 548-556.

[52] S. Dahlström, L. Davidson, Large eddy simulation of the flow around an Aerospatiale A-aerofoil, in: ECCOMAS 2000, European Congress on Computational Methods in Applied Sciences and Engineering, Barcelona, Spain, 2000.

[53] I. Solís-Gallego, K.M. Argüelles, J.M. Fernández Oro, S. Velarde-Suárez, Wall-Resolved LES Modeling of a Wind Turbine Airfoil at Different Angles of Attack, J. Mar. Sci. Eng. 8 (2020) 212-230.

[54] K. Asada, S. Kawai, Large-eddy simulation of airfoil flow near stall condition at Reynolds number 2.1×10^6, Phys. Fluids 30 (2018) 085103.

[55] H. Choi, P. Moin, Effects of the computational time step on numerical solutions of turbulent flow, J. Comput. Phys. 113 (1994) 1-4.

[56] F.R. Menter, Two-equation eddy-viscosity turbulence models for engineering applications, AIAA J. 32 (1994) 1598-1605.

[57] C. Zhang, H. Liu, F. Wang, W. Kong, Supercooled large droplet icing accretion and its unsteady aerodynamic characteristics on high-lift devices, Proc. Inst. Mech. Eng. G: J. Aerosp. Eng. 232 (2018) 1985-1997.

[58] S. Hosseinverdi, H.F. Fasel, Numerical investigation of laminar–turbulent transition in laminar separation bubbles: The effect of free-stream turbulence, J. Fluid Mech. 858 (2019) 714-759.

[59] L. Jenkins, M. Khorrami, M. Choudhari, Characterization of unsteady flow structures near leading edge slat: Part I: PIV measurements, in: 10th AIAA/CEAS Aeroacoustics Conference, American Institute of Aeronautics and Astronautics, 2004.

[60] C. Marongiu, P.L. Vitagliano, G. Zanazzi, R. Narducci, Aerodynamic analysis of an iced airfoil at medium/high Reynolds number, AIAA J. 46 (2008) 2469-2478.

[61] J.R. Brinkerhoff, M.I. Yaras, Numerical investigation of transition in a boundary layer subjected to favourable and adverse streamwise pressure gradients and elevated free stream turbulence, J. Fluid Mech. 781 (2015) 52-86.

[62] M. Gad-el-Hak, D.M. Bushnell, Separation control: Review, ASME J. Fluids Eng. 113 (1991) 5-29.

[63] J.K. Harvey, F.J. Perry, Flowfield produced by trailing vortices in the vicinity of the ground, AIAA J. 9 (1971) 1659-1660.

[64] N. Didden, C.M. Ho, Unsteady separation in a boundary layer produced by an impinging jet, J. Fluid Mech. 160 (1985) 235-256.

[65] G. Taherian, M. Nili-Ahmadabadi, M.H. Karimi, M.R. Tavakoli, Flow visualization over a thick blunt trailing-edge airfoil with base cavity at low Reynolds numbers using PIV technique, J. Vis. 20 (2017) 695-710.

[66] K.W. Cassel, A.T. Conlisk, Unsteady separation in vortex-induced boundary layers, Phil. Trans. R. Soc. Lond. A 372 (2014) 20130348.

[67] H.M. Gurbacki, M.B. Bragg, Unsteady flowfield about an iced airfoil, in: 42nd AIAA Aerospace Sciences Meeting, American Institute of Aeronautics and Astronautics, 2004.

[68] M. Mirzaei, M.A. Ardekani, M. Doosttalab, Numerical and experimental study of flow field characteristics of an iced airfoil, Aerosp. Sci. Technol. 13 (2009) 267-276.

[69] G.P.G. Silva, J.P. Eguea, J.A.G. Croce, F.M. Catalano, Slat aerodynamic noise reduction using dielectric barrier discharge plasma actuators, Aerosp. Sci. Technol. 97 (2020) 105642.

[70] W. Lu, P. Liu, H. Guo, T. Hu, Investigation on tones due to self-excited oscillation within leading-edge slat cove at different angles of attack: Frequency and intensity, Aerosp. Sci. Technol. 91 (2019) 59-69.

[71] M.D. Manshadi, M.K. Esfeh, Experimental investigation of flowfield over an iced aerofoil, Aeronaut. J. 120 (2016) 735-756.

[72] J. Jeong, F. Hussain, On the identification of a vortex, J. Fluid Mech. 285 (1995) 69-94.

[73] A.V. Oppenheim, Discrete-time signal processing, Pearson Education India, 1999.

[74] S. Gamard, W.K. George, Reynolds number dependence of energy spectra in the overlap region of isotropic turbulence, Flow Turbul. Combust. 63 (2000) 443-477.

[75] J.K. Eaton, J.P. Johnston, Low-frequency unsteadiness of a reattaching turbulent shear layer, in: Turbulent shear Flows III, Third International Symposium on Turbulent Shear Flows (1982) 162-170.

[76] M. Kiya, K. Sasaki, Structure of a turbulent separation bubble, J. Fluid Mech. 137 (1983) 83-113.

[77] N.J. Cherry, R. Hillier, M.E.M.P. Latour, Unsteady measurements in a separated and reattaching flow, J. Fluid Mech. 144 (1984) 13-46.